MECHANICAL, MATHEMATICAL AND COMPUTER MODELING IN PENETRATION MECHANICS – IV (HYBRID MODELS FOR NANOSTRUCTURED CERAMICS - II)

Principal Investigator: Valeriy V. Kartuzov

Contractor: Frantsevich Institute for Problems in Materials Science,
National Academy of Science of Ukraine

Contract Number: N62558-05-P-0488

Final Report

November 30, 2006

The research reported in this document has been made possible through the support and sponsorship of the U.S. Government through its European Research Office of the U.S. Approved for public release; distribution is unlimited.

Report Documentation Page

Form Approved
OMB No. 0704-0188

1. REPORT DATE	2. REPORT TYPE	3. DATES COVERED
30 NOV 2006		**00-11-2006 to 00-12-2006**

4. TITLE AND SUBTITLE	5a. CONTRACT NUMBER
MECHANICAL, MATHEMATICAL AND COMPUTER MODELING IN PENETRATION MECHANICS ? IV (HYBRID MODELS FOR NANOSTRUCTURED CERAMICS - II)	5b. GRANT NUMBER
	5c. PROGRAM ELEMENT NUMBER
6. AUTHOR(S)	5d. PROJECT NUMBER
	5e. TASK NUMBER
	5f. WORK UNIT NUMBER
7. PERFORMING ORGANIZATION NAME(S) AND ADDRESS(ES) **Frantsevich Institute for Problems in Materials Science,,National Academy of Science of Ukraine, , ,**	8. PERFORMING ORGANIZATION REPORT NUMBER
9. SPONSORING/MONITORING AGENCY NAME(S) AND ADDRESS(ES)	10. SPONSOR/MONITOR'S ACRONYM(S)
	11. SPONSOR/MONITOR'S REPORT NUMBER(S)

12. DISTRIBUTION/AVAILABILITY STATEMENT
Approved for public release; distribution unlimited

13. SUPPLEMENTARY NOTES
The original document contains color images.

14. ABSTRACT

15. SUBJECT TERMS

16. SECURITY CLASSIFICATION OF:			17. LIMITATION OF ABSTRACT	18. NUMBER OF PAGES	19a. NAME OF RESPONSIBLE PERSON
a. REPORT **unclassified**	b. ABSTRACT **unclassified**	c. THIS PAGE **unclassified**		**64**	

CONTENT

I. Numerical-analytical model of penetration of long elastically deformable projectiles into semi-infinite targets

Introduction

Penetration of non-deformable projectiles in continuum with various rheological properties has been of interest to researchers for a long time. The first modeling representations of penetration were formulated in XVIII-XIX centuries in Euler's, Poncelet's, Wuich's works, etc. Analysis of these results can be found in A.J. Sagomonjan's monographs [1,2].

In conjunction with development of more exact and effective technical means in last two decades the interest to this problem has considerably increased, and this is proved by works of Voejkova and Sagomonjan (1985) [3], Alojan (1985) [4], Liapykhin et al. (1993) [5], Bahrah et al. (1992) [6], Forrestal et al. (1988) [7], (1992) [8], (2000) [9], Dikshit and Sundararajan (1992) [10], Piekutowski et al. (1999) [11], Warren and Forrestal (1998) [12], Warren (2000) [13], Yossifon et al. (2001) [14], Chen and Li (2002) [15].

The analysis of modern state of the problem of analytical modeling of high-velocity penetration of non-deformable projectiles in target can be found in works by Forrestal et al. [7–9], Warren and Forrestal [12], Yarin et al. [16,17], Yossifon [14], Chen and Li [15]. From this analysis follows that at present there is a deficiency of relatively simple analytical models using natural physical and geometrical parameters of projectile and target and with a small number of fitting parameters.

In this study we have built and investigated a new model of penetration of non-deformable projectiles of various shapes in elastic-plastic and elastic-brittle materials.

The closest to the proposed model are models by Yarin et al. [16], Roisman et al. [17], Yossifon et al. [14] which use the method of peculiarities where equations of motion in elastic-plastic medium have a form of the Cauchy problem:

$$\left(m + A\left(x,\dot{x}\right)\right)\ddot{x} = B\left(x,\dot{x}\right)\dot{x}^2 + C(x,\dot{x}),\ x(0) = 0,\ \dot{x}(0) = -U_0. \qquad (1)$$

Here $U_0 > 0$ – initial projectile velocity, m – its mass, $x(t)$ – location of the tip of the projectile, and functions A, B, C have natural mechanical meaning (A – target added mass, B – drag coefficient, C – drag associated with plasticity). These functions are found analytically on the base of approximate solution of motion equations of elastic-plastic medium with appropriate boundary conditions. Equations (1) use exact velocity potential of ideal fluid in infinite domain for a projectile which shape is an ovoid of Rankine.

The comparison of full penetration depth of long non-deformable projectile, determined by our model for different velocities of impact with known experimental data shows that the experimental values of penetration depth appear less than theoretical ones. Similar results are demonstrated by the model suggested in [7,8] and based on a use of velocity field in material at expansion of spherical cavity. To adjust the theoretical results to experimental ones the authors in these works use a friction coefficient. Later, on the basis of the analysis of FEM-based calculations and experimental data [12], they neglect the influence of friction on penetration depth and develop the model that accounts for deformation rate in rheological equations of target material. Analyzing the influence of hardness of projectile material on experimental values of penetration depth in work [9] it is noted that harder projectiles have a slightly higher penetration depth than less hard ones. However, all experimental values of penetration depths are lower than theoretical depths for hard projectiles.

These facts led us to the necessity to take into account other possible effects, in particular, elastic deformation of projectile. In present study we investigate in uniaxial approximation the influence of forced elastic oscillations of projectile on key parameters of penetration process (penetration depth and velocity). It is shown, that elastic oscillations of projectile (usually neglected) have noticeable influence on penetration.

We also evaluate a critical velocity of impact at which the projectile undergoes plastic deformation causing irreversible changes of its shape and instability of its movement. The investigation of rigid-body motion and further analysis of forced elastic oscillations deals with impact velocities less then this critical velocity.

The main purpose of the present modeling investigation is:

– to build motion equations on the basis of velocity field in the target determined by a real projectile shape;

– to obtain deeper insight into the nature of target resistance to penetration of non-deformable and elastically deformable projectiles;

– to predict the dependence of projectile velocity *vs.* given geometrical and material parameters of projectile and target;

– to investigate the influence of projectile shape and its elastic oscillations on penetration;

– to compare results of model predictions with known experimental and calculated results.

1. Basic model equations of penetration of non-deformable projectiles into semi-infinite target

1.1. Geometrical scheme of penetration model of non-deformable projectile

Let's consider a normal penetration of axisymmetric projectile in semi-infinite target (see Fig.1).

In Fig. 1 we accept the following notations and assumptions: σ_1 — lateral surface of projectile (i. e. projectile surface without its rear surface), $\sigma_2 = \{x = 0,\ r \ge d/2\}$ — target free surface (assumed flat), $\sigma_3 = \{0 \le x \le (P - L),\ r = d/2\}$ — free surface of entry hole (assumed cylindrical). The direction of projectile motion coincides with axis x which is its axis of symmetry. At $P \le L$ surface σ_3 is absent.

Main model parameters are: $u(t)$ — projectile velocity; L — projectile length; $P(t) = \int_0^t u(\tau)d\tau$ — penetration depth; d — projectile diameter; U_s — striking (impact) velocity.

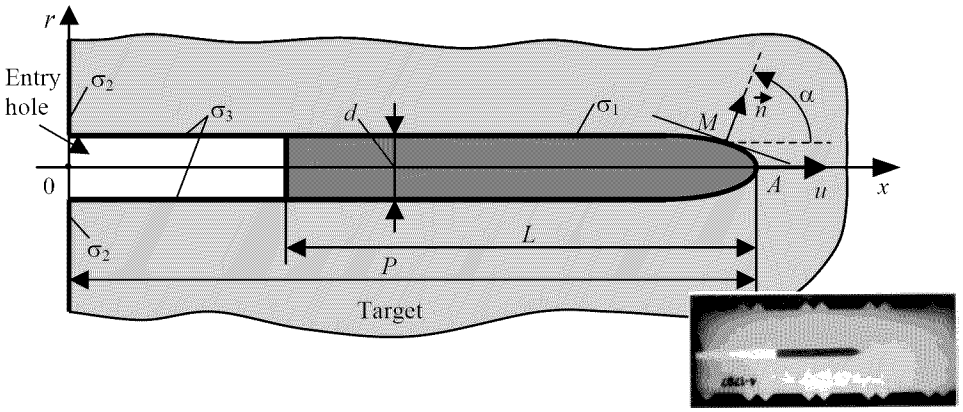

Fig. 1 Scheme of normal penetration of axisymmetric elongated non-deformable projectile in cylindrical system of coordinates $0r\theta x$

1.2. Velocity field in target

Velocity field in the vicinity of projectile is approximated by the field of velocities $\vec{v}$ for irrotational motion of ideal incompressible fluid. Defining $\vec{v}$ we assume, that a free surface of target $\sigma_2 = \{x = 0,\ r \ge d/2\}$ remains flat during penetration, and a free surface of entry hole σ_3 formed by a tail part of projectile is cylindrical: $\sigma_3 = \{r = d/2,\ 0 \le x \le (P - L)\}$, (see Fig. 1).

As it is known [18,19] the equations of non-stationary irrotational movement of ideal incompressible fluid with density ρ in case of potential flow have the following form:

$$\nabla^2\Phi = 0, \qquad \text{Laplace equation} \tag{2}$$

$$\rho(\partial\Phi/\partial t) + \rho/2|\text{grad}\Phi|^2 + p = f(t), \text{ Lagrange-Cauchy integral} \tag{3}$$

where $\Phi(x,r,t,P)$ – velocity potential (i.e. $\vec{v} = -\text{grad}\Phi$), p – static pressure component, $f(t)$ – arbitrary function of time, independent from coordinates and identical over the whole volume of fluid. Function $f(t)$ is found from boundary conditions.

First equation (2) is a condition of incompressibility of fluid (or the continuity equation), second equation (3) – the first integral of Euler's equation of motion which is known as Lagrange-Cauchy integral (sometimes it is called Bernoulli-Cauchy integral). Equation (3) is conservation of momentum and $\text{grad}[\rho(\partial\Phi/\partial t) + \rho/2|\text{grad}\Phi|^2 + p] = \text{div}\sigma' = \text{grad}(f(t))$ where σ' is a deviatoric part of the Cauchy stress as described by Yarin et al [16]. If Lagrange-Cauchy integral (3) is considered on projectile surface left part of equation (3) defines a normal pressure p_c of target material on projectile surface, i.e. $p_c = \rho(\partial\Phi/\partial t) + \rho/2|\text{grad}\Phi|^2 + p$.

Due to the assumptions made and because equation (2) does not contain partial derivative with respect to time, time t enters into (2) as a parameter which influence is manifested through the boundary conditions containing geometrical characteristics of projectile and its velocity $u(t)$. Therefore, both time and depth of penetration $P(t)$ are listed in the arguments of potential Φ.

Thus, for potential Φ we have the following Neumann boundary conditions:

$$\partial\Phi/\partial n = -u(t)n_x \text{ at } M(r,x)\in\sigma_1,\ \partial\Phi/\partial n = 0 \text{ at } M(r,x)\in(\sigma_2 \cup \sigma_3), \tag{4}$$

$$\Phi = O(1/R)\to 0 \text{ when } R = \sqrt{r^2 + x^2} \to \infty,$$

where σ_1, σ_2, σ_3 — surfaces as indicated earlier, n_x — cosine of angle α between axis x and normal to projectile surface σ_1, (see Fig. 1). Condition (4) is the condition of impenetrability of target material across projectile surface σ_1, cylindrical surface σ_3, and target surface σ_2.

From the linearity of boundary problem of Neumann (2), (4) follows, that velocity potential $\Phi(x,r,t,P)$ may be presented as

$$\Phi(x,r,t,P) = u(t)\varphi(x,r,P). \tag{5}$$

Here function $\varphi(x,r,P)$ is a solution of Laplace equation

$$\nabla^2\varphi = 0 \tag{6}$$

with boundary conditions

$$\partial\varphi/\partial n = -n_x \text{ when } M(x,r)\in\sigma_1,\ \partial\varphi/\partial n=0 \text{ at } M(x,r)\in(\sigma_2 \cup \sigma_3),\ \varphi = O(1/R)\to 0 \text{ when } R\to\infty. \tag{7}$$

Let's notice, that $\varphi(x, r, P)$ depends on P as on parameter, which, in its turn, depends on time t.

Thus, the field of velocities $\vec{v}$ in the proposed model is defined by an expression

$$\vec{v} = -u(t)\ \text{grad}\ \varphi(x, r, P). \tag{8}$$

Obviously, velocity field (8) is approximate, since during penetration a free surface of target σ_2 does not remain plane and a free surface of input hole σ_3 is not a circular cylinder (see Fig. 1). In a complete formulation of penetration problem of rigid projectile the shape of these surfaces has yet to be determined.

However, according to the experiments (for example, Piekutowski et al, 1999 [11]) the deviations from surfaces σ_2 and σ_3 accepted in the proposed model are insignificant (in comparison with a diameter of projectile), especially it concerns plastic materials (see, for example, X-ray photo from the mentioned work, Fig. 1). Thus, the accepted assumptions as to surfaces σ_2 and σ_3, in our point of view, insignificantly distort actual field of velocities $\vec{v}$, but considerably simplify the investigation of this field and emphasize its main features.

Let's note, that in the proposed model the function $\Phi = u\varphi$ is a velocity potential of ideal incompressible fluid for which there are no friction forces (tangential stresses) between target material and projectile surface. This approximation, which neglects tangential stresses on projectile surface, is a common one in the majority of computing schemes. As was mentioned earlier, in [12] on the base of computational modeling and experimental evidence authors rejected the use of sliding friction.

Because of this, we believe that a prediction of integral values of penetration process (such as a force that decelerates projectile, penetration depth and velocity) which use velocity field (8) can be quite satisfactory. Moreover, as the main influence on projectile motion is rendered by potential $\Phi = u\varphi$ and velocity $\vec{v} = -u\text{grad}\varphi$ on the surface of a head part of projectile, then the influence of boundary conditions (7) on σ_2 and σ_3 would decrease as penetration depth P increases and become insignificant when P would exceed several projectile head lengths.

1.3. Ballistic integro differential equations of projectile motion

As in [20], for building of projectile motion equation we use Lagrange-Cauchy (3). If we substitute velocity potential (5) ($\Phi = u(t)\varphi(M,P)$, $P = \int_0^t u(\tau)d\tau$, $\frac{\partial\Phi}{\partial t} = \varphi\frac{du}{dt} + \varphi'_P u^2$, $\text{grad}\Phi = u\text{grad}\varphi$) in Lagrange-Cauchy integral (3) and consider this integral on projectile surface, then a left-hand part of (3) would define a contact pressure $p_c(M,P)$ of target material on projectile. Here coefficient φ'_P takes into account change of the target boundary with penetration, i. e. domain of definition of velocity field (8). Therein lies its mechanical significance. Further we assume that in (3) static components of pressure on projectile surface $p = R_t$ where R_t — pressure in a spherical cavity during its quasi-static expansion, i.e. here we use the analytical solution of a problem of quasi-static expansion of spherical cavity in target material which takes into account elastic and plastic (or brittle) response of material. R_t is constant and depends on mechanical properties of target material only (see (16–19)). The use of such solution is caused by a fact that analytical solution of quasi-static indentation of rigid projectile of real shape in target material generally is not possible. Besides, since target material at this indentation flows or fractures and relaxation of stresses takes place, value R_t (as it will be shown further) enters into the equation of projectile motion as integrand. This, in our opinion, makes the adopted approximations justified and sufficient.

Thus, on the basis of Lagrange-Cauchy integral (3) for normal dynamic pressure of target material $p_c(M,P) = \rho\frac{\partial\Phi}{\partial t} + \frac{1}{2}\rho\left|\text{grad}\,\Phi\right|^2 + p$ on projectile in point M on its surface we obtain

$$p_c(M,P) = \rho\varphi(M,P)\frac{du}{dt} + \left(\left|\text{grad}\,\varphi(M,P)\right|^2 + 2\varphi'_P(M,P)\right)\frac{\rho u^2}{2} + R_t, \tag{9}$$

where $P = \int_0^t u(\tau)\,d\tau$ — projectile penetration depth.

A full decelerating force N acting on projectile is obtained by integration on a contact surface of projectile and target $\sigma(P)$ of a projection $(-p_c(M,P)\cdot n_x(M,P))$ of contact pressure (9) onto axis x. Here $n_x(M,P)$ — a cosine of an angle which is formed by unit normal to projectile surface in point M with axis x (see Fig. 1).

Equating a complete force of resistance to projectile N to its inertia force $m\frac{du}{dt}$ (m — projectile mass) the ballistic equation of motion of non-deformable projectile is obtained:

$$m\frac{du}{dt} = N, \quad u(0) = U_0, \tag{10}$$

where $U_0 = U_s$ — impact velocity.

Accounting for (9), equation (10) can be written as

$$m\frac{du}{dt} = -\rho A(P)\frac{du}{dt} - B(P)\frac{\rho u^2}{2} - C(P)R_t,\ u(0) = U_0. \tag{11}$$

In (11) the coefficients A, B, C depend on projectile shape, penetration depth P and are defined by the formulas

$$A(P) = \int_{\sigma(P)} \varphi(M,P)n_x(M,P)\,d\sigma_M\ ,\ C(P) = \int_{\sigma(P)} n_x(M,P)\,d\sigma_M\ , \tag{12}$$

$$B(P) = \int_{\sigma(P)} \left(\left|\operatorname{grad}\varphi(M,P)\right|^2 + 2\varphi'_P(M,P)\right)n_x(M,P)\,d\sigma_M\ .$$

In these formulas a contact surface $\sigma(P)$ of projectile and target in a moment of time t is approximately defined by the inequality

$$\sigma(P) = \left(M : \rho\varphi(M,P)\frac{du}{dt} + \left(\left|\operatorname{grad}\varphi(M,P)\right|^2 + 2\varphi'_P(M,P)\right)\frac{\rho u^2}{2} + R_t > 0\right). \tag{13}$$

If projectile surface is formed by a rotation of line $r = r(x)$ around axis x (see Fig. 2), then in (12)

$$n_x = -\frac{r'}{\sqrt{1+(r')^2}}, \qquad d\sigma_M = 2\pi r\sqrt{1+(r')^2}\,dx,$$

and these formulas can be written as:

$$\begin{aligned} A(P) &= -2\pi\int_{l_P} \varphi(x,r(x),P)r(x)r'(x)\,dx, \qquad C(P) = -2\pi\int_{l_P} r(x)r'(x)\,dx, \\ B(P) &= -2\pi\int_{l_P}\left(\left|\operatorname{grad}\varphi(x,r(x),P)\right|^2 + 2\varphi'_P(x,r(x),P)\right)r(x)r'(x)\,dx, \end{aligned} \tag{14}$$

where a stroke denotes derivative with respect to x, and l_P — intervals on axis x which define a region of contact of projectile and target material:

$$l_P = \left\{x : \rho\varphi(x,r(x),P)\frac{du}{dt} + \left(\left|\operatorname{grad}\varphi(x,r(x),P)\right|^2 + 2\varphi'_P(x,r(x),P)\right)\frac{\rho u^2}{2} + R_t > 0\right\}. \tag{15}$$

Fig. 2 illustrates one contact interval $l_P = [x_c,P]$.

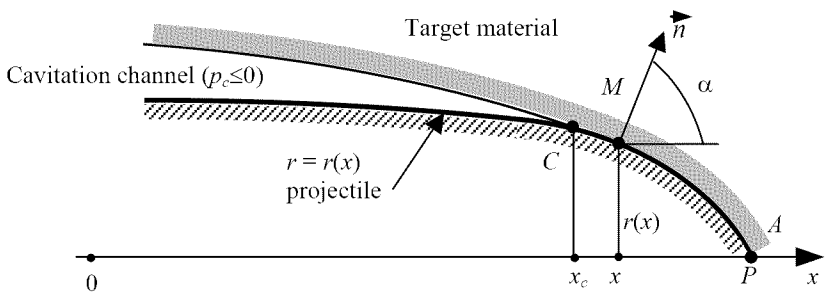

Fig. 2 To the definition of contact surface between projectile and target material; C — point of separation of target material from projectile surface

Inequalities (13) and (15), approximately determining contact surface $\sigma(P)$ between projectile and target material, are more detailed form of the condition $p_c(M) > 0$. Regions of separation of target material from projectile surface $\sigma(P)$ are approximately defined by a condition: $\sigma(P) = \{M: p_c \le 0\}$.

As it was noted earlier, the value of static penetration resistance of target material R_t is defined by the analytical solution of the problem of expansion of a spherical cavity. At present there exist a number of solutions for both brittle and plastic materials. Several of them that are used further we list below.

For elastic-ideally plastic and elastic-brittle materials the following formulas can be used respectively [21-23]:

$$R_t = \frac{2}{3} Y \left(1 + \ln \left(\frac{E}{3Y(1-\nu)} \right) \right), \tag{16}$$

$$R_t = Y \left[\frac{E}{3Y\left(1-(1-\nu)\sqrt{\sigma_f/(2Y)}\right)} \right]^{2\alpha/3}. \tag{17}$$

Here E, ν are Young's modulus and Poisson's ratio, Y — compressive yield strength for (16) and strength at uniaxial compression for (17), σ_f — tensile strength, α — characteristic of fractured media [23]. To account for a post-yield strain-hardening of material the following formulas can be used [8,12]

$$R_t = \frac{2}{3} Y \left(1 + \left(\frac{2E}{3Y} \right)^n I \right), \quad I = \int_0^{1-3Y/(2E)} \frac{(-\ln x)^n}{1-x} dx, \tag{18}$$

where n — strain hardening exponent.

For penetration of in limestone Frew [24] established that penetration resistance depends on penetrator dimensions:

$$R_t = \Psi + \phi\,(a_0/a), \tag{19}$$

where $\Psi = 607$ MPa, $\phi = 86$ MPa, $2\,a_0 = 25.4$ mm, a — projectile radius (mm).

1.4. Determination of velocity potential φ by method of boundary integral equations [25]

The solution of the Neumann problem (6), (7) is sought as a potential of a simple layer

$$\varphi(M,P) = \int_{\bar{S}} \frac{\mu(M_1)}{R(M,M_1)} dS(M_1), \; M \in (\bar{D} \cup \bar{S}), \; M_1 \in \bar{S}, \tag{20}$$

in which $\bar{S} = (S \cup S')$ — a surface symmetric to plane $x = 0$, and $\bar{D}$ — infinite area with a boundary $\bar{S}$; $R(M,M_1)$ — distance between a fixed point of observation $M(x,r,\theta)$ and a source point of integration $M_1(x_1,r_1,\theta_1)$ (see Fig. 3); $\mu(M_1)$ — the unknown density of simple sources distributed on surface $\bar{S}$.

The density $\mu(M_1)$ is a solution of the following boundary integral equation

$$\mu(M) + \frac{1}{2\pi} \int_{\bar{S}} \mu(M_1) \frac{\cos(\vec{R},\vec{n})}{R^2(M,M_1)} dS(M_1) = \frac{1}{2\pi} g(M), \quad M, \; M_1 \in \bar{S}, \tag{21}$$

$$g(M) = \begin{cases} \dfrac{x}{|x|} \cdot n_x(M), & M \in \sigma_1 \cup \sigma_1', \\ 0, & M \in \sigma_3 \cup \sigma_3', \end{cases} \tag{22 a-b}$$

where vector $\vec{R}$ is directed from point M to M_1, $\vec{n}(M)$ — unit normal to $\bar{S}$ in point M (internal with respect to $\bar{D}$), $n_x(M)$ — a projection of a normal $\vec{n}$ onto axis x.

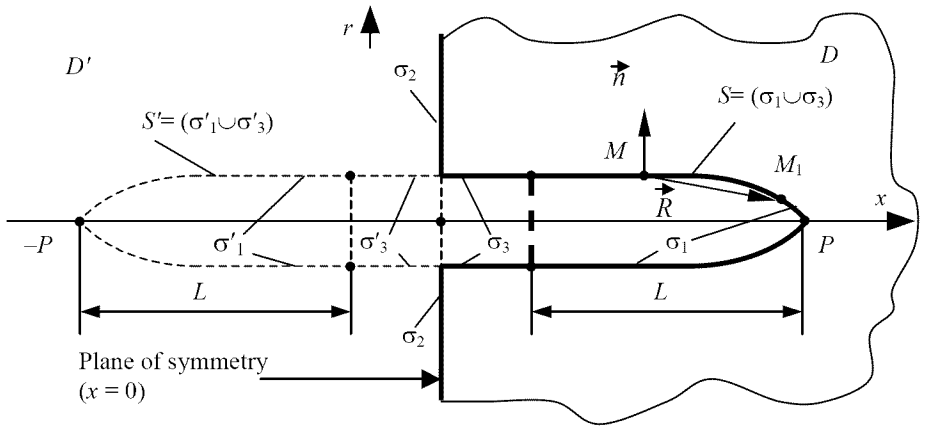

Fig. 3 Geometrical scheme of the domain of definition $\overline{D} = D \cup D'$ for potential φ. Region D' and surface $S' = (\sigma'_1 \cup \sigma'_3)$ are symmetric to region D and surface $S = (\sigma_1 \cup \sigma_3)$ with respect to plane $x = 0$.

If surface $\overline{S}$ is formed by a rotation of line $r = r(x)$, $x \in [-P,P]$ around axis x and symmetry to a plane $x = 0$ and axis x is taken into account as well, then boundary equation (21) can be written as

$$\mu(x) + \frac{2}{\pi}\int_0^P \left[\tilde{K}(x,x_1) + \tilde{K}(x,-x_1)\right]\mu(x_1)\,dx_1 = \frac{g(x)}{2\pi}, \quad x, x_1 \in [0,P],$$

$$g(x) = \begin{cases} 0, & x \in [0, P-L[, \\ -\dfrac{r'}{\sqrt{1+r'^2}}, & x \in [0,P] \setminus [0, P-L[. \end{cases}$$

Here we have the following notations:

$$\tilde{K}(x,x_1) = \left(\frac{E(m)\left[(x-x_1)n_x + (r-r_1)n_r\right]}{(a-b)\sqrt{a+b}} - \frac{E(m)-K(m)n_r}{2r\sqrt{a+b}} \right) r_1 \sqrt{1+r_1'^2},$$

$a = r^2 + r_1^2 + (x-x_1)^2$, $b = 2rr_1$, $r = r(x)$, $r_1 = r(x_1)$, $m = \dfrac{2b}{a+b}$, K — full elliptic integral of the first order, E — full elliptic integral of the second order [26], $n_r(M)$ — a projection of normal $\vec{n}$ to axis r (see. Fig. 3).

For components of velocity $v_x = -u(t)\dfrac{\partial \varphi}{\partial x}$, $v_r = -u(t)\dfrac{\partial \varphi}{\partial r}$ in directions x, r (see Fig. 1), respectively, we obtain

$$v_x(x,r) = 4u(t)\int_{-P}^{P} \frac{E(m)(x-x_1)}{(a-b)\sqrt{a+b}} r_1 \sqrt{1+r_1'^2}\,\mu(x_1)\,dx_1,$$

$$v_r(x,r) = 4u(t)\int_{-P}^{P} \left[\frac{E(m)\left(2r^2-a\right)}{2r(a-b)\sqrt{a+b}} + \frac{K(m)}{2r\sqrt{a+b}} \right] r_1 \sqrt{1+r_1'^2}\,\mu(x_1)\,dx_1. \qquad (23)$$

2. An approximate account of elastic oscillations of long projectiles and estimation of value of impact velocity at which a projectile undergoes a plastic flow

Further, while evaluating the influence of elastic oscillations of long projectile on its penetration, we neglect local elastic deformations of projectile nose and assume that the projectile has the shape of circular cylinder with a diameter d and length L. These oscillations are considered separately from projectile motion as a rigid body and the estimate of their influence on the transportation velocity of penetrator is made via energy loss. To evaluate the influence of forced elastic oscillations of projectile we use a solution of a problem of longitudinal oscillations of a rod [27,28] with one free end ($x = 0$), and compressive stresses ($-\sigma_0$) instantly applied to another ($x = L$) (at the moment of time $t = 0$):

$$w=-\left\{\frac{\sigma_0 t^2}{2\rho_p L}+\frac{2\sigma_0 L}{\pi^2 E_p}\sum_{i=1}^{\infty}\frac{(-1)^i}{i^2}\left[1-\cos\frac{i\pi c_0 t}{L}\right]\cos\frac{i\pi x}{L}\right\},\quad i=1,2,3,\ldots, \tag{24}$$

where $w(x,t)$ — relative displacement of cross-section of a rod x at the moment of time t, ρ_p — density of rod material, E_p — Young's modulus of rod material, $c_0=\sqrt{E_p/\rho_p}$ — sound speed in projectile. The influence of cross-section oscillations is neglected. We believe the use of this solution is justified since (as the calculations show, see Fig.8) a penetration of long rigid projectile occurs at almost constant acceleration (du/dt) and, thus, at almost constant braking force $N=-m\frac{du}{dt}=\frac{\sigma_0\pi d^2}{4}>0$, acting on projectile (here u — solution of initial boundary problem (11)). Besides, the value of force N weakly changes at small variations of initial condition $u(0)=U_0$ in (11).

Let's note, that in this paragraph for convenience it is supposed, that the force compressing projectile N is positive, unlike (10).

From (24) for displacement w and velocity $\dot{w}$ at $x=L$ (i.e. for w and $\dot{w}$ at projectile tip caused by its forced oscillations with a period $\tau=2L/c_0$) we obtain

$$w(L,t)=-\frac{\sigma_0 c_0}{E_p}t,\ \dot{w}=\frac{\partial w}{\partial t}=-\frac{\sigma_0 c_0}{E_p}. \tag{25}$$

Here $\sigma_0=\frac{4N}{\pi d^2}$ and braking force $N>0$ is a little changing value ($N\approx const$ through a whole depth of penetration); vectors w and $\dot{w}$ are directed opposite to the direction of projectile motion. Therefore the initial velocity of projectile penetration U_0 in the target is

$$U_0=U_s+\dot{w}=U_s-\frac{\sigma_0 c_0}{E_p}=U_s-\frac{4Nc_0}{\pi d^2 E_p}, \tag{26}$$

where U_s — projectile velocity before its meeting with target, i.e. impact velocity. For a non-deformable projectile $U_0=U_s$.

On the basis of (24) a longitudinal deformation of projectile $\partial w/\partial x$ (caused by oscillations) at the moment of time t is defined by

$$\frac{\partial w}{\partial x}=\frac{2\sigma_0}{\pi E_p}\sum_{i=1}^{\infty}\frac{(-1)^i}{i}\left[1-\cos\frac{i\pi c_0 t}{L}\right]\sin\frac{i\pi x}{L},\quad i=1,2,3,\ldots. \tag{27}$$

For the moments of time $t=\frac{L}{c_0}(2i-1)$ this deformation $\frac{\partial w}{\partial x}=-\frac{\sigma_0}{E_p}=const<0$ at all values $x\in[0,L]$. Therefore during these moments of time projectile is entirely compressed by stresses ($-\sigma_0$), i.e. in each cross-section of projectile x there exists compressing stress ($-\sigma_0$).

During an impact the energy of projectile consists from: a kinetic energy $T=\frac{1}{2}mu^2$ (u — projectile transportation velocity); elastic energy W_1 caused by lateral compression of projectile; energy of elastic oscillations of projectile W_2, caused by sudden application of braking force N.

The elastic energy W_1 associated with lateral transversal compression of projectile by pressure

$$p_l=p_c(M,P)\sin\alpha=\left(\rho\varphi(M,P)\frac{du}{dt}+\left(\left|\operatorname{grad}\varphi(M,P)\right|^2+2\varphi'_P(M,P)\right)\frac{\rho u^2}{2}+R_t\right)\sin\alpha,$$

where point M is on a lateral surface of projectile and α — an angle which forms a normal to projectile surface in point M with its axis, p_c — normal pressure of target material on projectile surface, see (9), is approximately estimated by the formula

$$W_1=\begin{cases}\int_0^P e(p_l)\,dx, & P<L,\\ \int_0^L e(p_l)\,dx, & P\ge L.\end{cases} \tag{28}$$

Here $e(p_l)=\dfrac{\pi d^2(1-\nu_p)}{4E_p}p_l^2(M,P)$ — energy of deformation of projectile cross-section in point M at penetration depth P, determined in the assumption, that normal stress in projectile cross-sections is absent (ν_p — Poisson ratio for projectile material). Estimating p_l we assume $\sin\alpha = 1$.

Energy of forced elastic longitudinal oscillations of projectile W_2 accumulated to the moment of time t (work of drag force spent on elastic oscillations) on the basis of (25) is estimated by value

$$W_2=\frac{1}{2}Nw(L,t)=\frac{2N^2c_0}{\pi d^2E_p}t=\frac{\pi d^2\sigma_0^2c_0}{8E_p}t, \tag{29}$$

which coincide with value [27] where it is represented by a convergent series. From (29) can be seen that the energy of forced oscillations increases proportionally to time while braking force remains constant.

Since $p_l \le \sigma_0=\dfrac{4N}{\pi d^2}$, then for energy W_1 we obtain an estimation

$$W_1 \le \frac{4(1-\nu_p)N^2L}{\pi d^2E_p}.$$

From this and from (29) at $c_0t >> 2L$ we obtain $W_1 << W_2$ and we can neglect the energy of transverse compression. Further calculations confirm that we can neglect this energy.

Solution of equation (11) at initial condition (26) we denote as $\overline{u}$ and further refer to it as "a velocity of penetration of quasi-rigid projectile". This can be justified by the fact that initial condition (26) for the equation of motion of non-deformable projectile (11) takes into account projectile elastic deformations.

Thus, between kinetic energy of quasi-rigid projectile $T=\dfrac{1}{2}m\overline{u}^2$ and complete energy of deformable projectile $\dfrac{1}{2}mu^2+W_1+W_2$ there is a relationship

$$\frac{1}{2}m\overline{u}^2=\frac{1}{2}mu^2+W_1+W_2,$$

which defines penetration velocity u of deformable projectile through quasi-rigid projectile velocity $\overline{u}$

$$u=\overline{u}\sqrt{1-\frac{2(W_1+W_2)}{m\overline{u}^2}}, \tag{30}$$

where values W_i, i = 1,2, are calculated by formulas (28), (29) and depend on braking force $N=-m\dfrac{du}{dt}$, which is approximately defined by Cauchy problem (11) and (as it was discussed earlier) weakly changes during an impact. Thus, with a sufficient accuracy one may also assume $N\approx -m\dfrac{d\overline{u}}{dt}$. If we neglect energy W_1, then formula (30) takes simple form

$$u=\overline{u}\sqrt{1-\frac{2W_2}{m\overline{u}^2}}. \tag{30′}$$

From (30) follows, that a motion of projectile (as a solid body) with transportation velocity u takes place until the moment of time t^* when the following equality comes true

$$2(W_1+W_2)=m\overline{u}^2.$$

It means that a penetration of projectile stops when its kinetic energy $\dfrac{1}{2}mu^2$ becomes zero and it has only the energy of its elastic deformation. After this moment a transportation motion of projectile stops and it performs damped oscillations.

Having defined a transportation motion of projectile $u(t)$ by (30) for a complete actual penetration depth P we obtain

$$P=\int_0^{t^*}u(\tau)d\tau,$$

and for a correction ΔP to a final penetration depth of quasi-rigid projectile $\overline{P}$ we have

$$\Delta P = P - \overline{P} = \int_0^{t^*} u(\tau)d\tau - \int_0^{t^{**}} \overline{u}(\tau)d\tau < 0,$$

where t^{**} — time of impact of quasi-rigid projectile ($t^* \le t^{**}$).

Let evaluate a threshold value of impact velocity $U_s = U_{sC}$ at which a projectile undergoes plastic deformations causing irreversible changes of its shape and instability of motion.

Since σ_0 — peak value of an axial stress in projectile (if a projectile does not lose stability at compression) the plastic deformations in it start to develop under a condition

$$\sigma_0 = \frac{4N}{\pi d^2} = Y_p, \tag{31}$$

where Y_p — dynamic yield stress of projectile material.

If we take into account $N = -m\frac{du}{dt} = \frac{m}{m + \rho A(P)}\left(B(P)\frac{\rho u^2}{2} + C(P)R_t\right)$ (see equation (11)), then from (31) we obtain the following equation for projectile velocity u at which the plastic deformations appear in it

$$\frac{\pi d^2\left(m + \rho A(P)\right)}{4m}Y_p = B(P)\frac{\rho u^2}{2} + C(P)R_t,$$

or

$$u = \sqrt{\frac{\pi d^2}{2\rho B(P)}\left(\left(1 + \frac{\tilde{m}}{m}\right)Y_p - \frac{4C(P)}{\pi d^2}R_t\right)}, \tag{32}$$

where $A(P)$, $B(P)$, $C(P)$ — coefficients of the equation (11) and $\tilde{m} = \rho A(P)$ — an added mass. Let's note here, that the coefficients A, B, C depend on penetration depth P (as parameter) and shape of the projectile nose. At sufficiently large values of P (for projectiles discussed further $P > L_h$, L_h — length of a head part of projectile) they are constant (do not depend on P and depend only on projectile shape). Therefore for these values P and the right-hand part of equality (32) is a constant value. Besides, as further calculations show, this constancy is almost established by the moment of returning of a front of elastic longitudinal wave ($t = \frac{2L}{c_0}$) in projectile to a contact surface. Therefore further factors A, B, C are considered as constants, and argument P is not referred to in formulas.

As the largest value of velocity u is observed at the beginning of impact, when $u \approx U_s - \frac{\sigma_0 c_0}{E_p} = U_s - \frac{Y_p c_0}{E_p}$ (see (26) and (31)), for critical velocity of projectile U_{sC} till its meeting with a target (i.e. for critical velocity of impact) from (32) we obtain the estimate

$$U_{sC} = \frac{Y_p c_0}{E_p} + \sqrt{\frac{\pi d^2}{2\rho B}\left(\left(1 + \frac{\tilde{m}}{m}\right)Y_p - \frac{4C}{\pi d^2}R_t\right)}, \tag{33}$$

and projectile flows under a condition $U_s \ge U_{sC}$. Thus, plastic deformations in projectile develop from the beginning of impact. In formula (33) radicand has to be positive. If this expression is negative, i.e. the opposite inequality is true

$$\left(1 + \frac{\tilde{m}}{m}\right)Y_p - \frac{4C}{\pi d^2}R_t \le 0, \tag{34}$$

which means that the target is of the same strength as the projectile or even stronger, then critical velocity of impact is

$$U_{sC} = \frac{Y_p c_0}{E_p},$$

and projectile flows under a condition of $U_s \ge U_{sC}$ which coincides with known condition [29]. Thus, the condition $U_s \ge U_{sC}$ where U_{sC} is defined by (33), is a generalization of this known condition of transition of the projectile material into a plastic state.

For long projectiles when $\frac{\tilde{m}}{m} = \frac{\rho\overline{A}}{\rho_p L} << 1$, $\overline{A} = \frac{4A}{\pi d^2}$ and $\overline{C} = \frac{4C}{\pi d^2} \approx 1$, inequality (34) simplifies and has a simple mechanical meaning: $R_t \ge Y_p$.

If we introduce "reduced strengths" of projectile and target, respectively,

$$\overline{R}_t = \overline{C} R_t, \quad \overline{Y}_p = \left(1 + \frac{\rho \overline{A}}{\rho_p L}\right) Y_p, \tag{35}$$

and denote $\overline{B} = \dfrac{4B}{\pi d^2}$, then formula (33) for critical velocity can be rewritten as

$$U_{sC} = \begin{cases} \dfrac{Y_p c_0}{E_p} + \sqrt{\dfrac{2}{\rho \overline{B}}\left(\overline{Y}_p - \overline{R}_t\right)} & , \ \overline{Y}_p \geq \overline{R}_t, \\ \dfrac{Y_p c_0}{E_p}, & \overline{Y}_p < \overline{R}_t, \end{cases} \tag{36}$$

and is analyzable by elementary means. Indeed: if value Y_p increases, then critical velocity U_{sC} increases also; if strength of target R_t falls, this speed increases; if sharpness of projectile nose increases the coefficient $\overline{B}$ decreases (for spherical ($\psi = 0.5$) nose $\overline{B} = 0.58$, for ogival ($\psi = 3$) nose $\overline{B} = 0.11$) and, hence, U_{sC} increases; if bluntness of the nose increases the coefficient $\overline{A}$ increases (for ogival nose $\overline{A} = 0.0010$, for spherical $\overline{A} = 0.0015$) and, therefore, the reduced strength of projectile $\overline{Y}_p$ (associated with the added mass $\tilde{m} = \rho A$, see (35)) increases. Formula (36) can be used to define a dynamic yield stress of projectile material Y_p if other values entering into it are known. See example in appendix.

Note, that the case of stability loss of long projectile can be also considered under the proposed scheme of investigation of plastic deformations of projectile. Indeed, in this case in the main formulas (31) — (36) it is necessary to change value Y_p for the value of critical stress $Y_c = \varphi Y_p$ where $\varphi < 1$ — coefficient of a longitudinal bend for centrally compressed rod (projectile) which depends on its flexibility λ, as well as on properties of projectile material. The characteristic type of a dependence of normalized critical stress $\varphi = \dfrac{Y_c}{Y_p}$ vs. flexibility λ is presented in Fig. 4 [30].

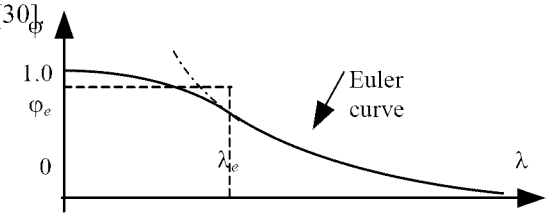

Fig. 4 A characteristic type of a dependence of a coefficient of longitudinal bend $\varphi = \dfrac{Y_c}{Y_p}$ vs. flexibility λ (the normalized diagram of a critical stress [30]). For values $\lambda \geq \lambda_e$ the loss of stability occurs at elastic deformations; for values $\lambda < \lambda_e$ the loss of stability occurs at elastic-plastic deformations.

We believe, that flexibility of projectile can be estimated as $\lambda = \dfrac{4L}{d}$ in the initial, most dangerous for projectile, moment of impact when lateral surface of projectile is unconstrained and the compressing stresses ($-\sigma_0$) appear in its any cross-section.

Thus it is easy to understand that the loss of stability leads to a decrease of value of critical velocity U_{sC} (since $\varphi < 1$) (see (33), (36)), especially for long projectiles.

3. Numerical implementation

We consider the case of elastic deformation of the projectile and compare the results with experimental data where penetrator was only in linearly-elastic state (it was controlled by a post-impact projectile state).

As an illustration, the penetration of projectile is calculated with a geometry given in Fig.5. Equation (11) was solved using Euler's method. For the considered projectile shapes and velocity range, the calculations by formula (9) show that $p_c > 0$ on the projectile surface and there is no separation of material from projectile (see Fig. 2). The estimate of elastic energy from transversal compression W_1 by formula (28) shows that it can be neglected.

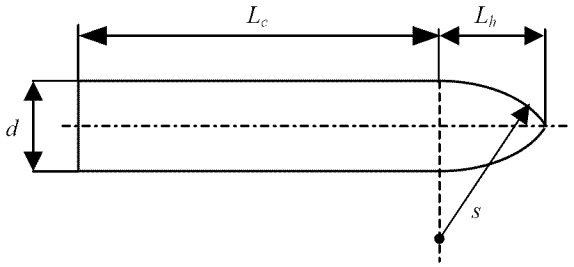

Fig. 5 Geometry of ogival projectile, $s = 3d$, $L_h = 11.8$ mm for ogival head, $s = 0.5\ d$, $L_h = 3.555$ mm for spherical head, $L_c = 59.3$ mm, $d = 7.11$ mm, $L = L_c + L_h$.

In Fig.6 the plots of potential φ at the projectile tip changing with penetration depth are demonstrated. The dependence of derivative φ'_P vs. P for point A (Fig. 1) on the projectile surface is shown in Fig.7.

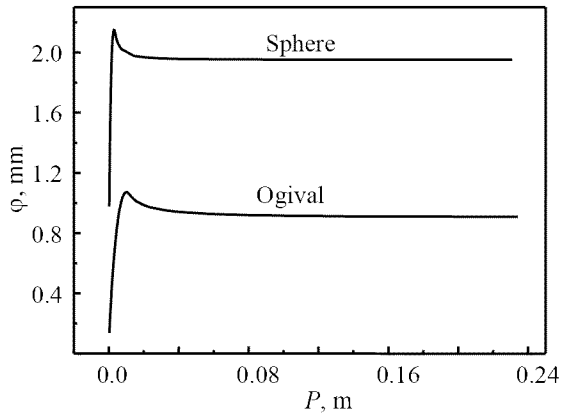

Fig. 6 Dependence of potential at projectile tip on penetration depth

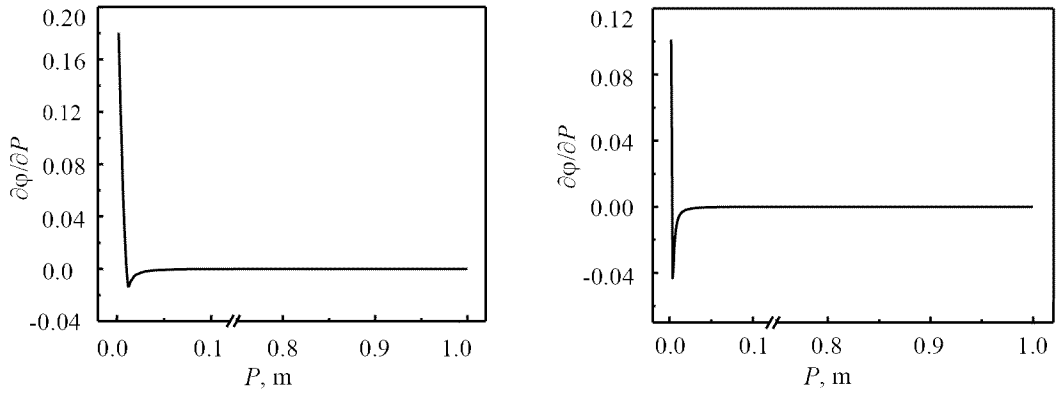

Fig. 7 Dependence of derivative φ'_P vs. P for ogival (a) and spherical (b) nose projectiles

The dependencies of the coefficients A, B, C of equation (11) on penetration depth P are shown in Fig.8. Figure 9 shows the dependence of penetration velocity u vs. time t. Curve 1 here is the solution of (11) for $U_0 = U_s$, curve 2 is the solution of (11) with initial condition (26), curve 3 is calculated using (30′). Figure 10 demonstrates the dependence of penetration velocity u vs. time t and penetration depth P for ogival and spherical nose. The dependence of penetration depth P on time t is given in Fig.11. The typical fields of velocities in target material for spherical and ogival heads are illustrated in Fig.12 and 13 for penetration depth 37.0 mm and 35.9 mm respectively. In the vicinity of projectile head these fields have explosive character. R_t defined by (16) was used in all calculations in Fig. 9—13.

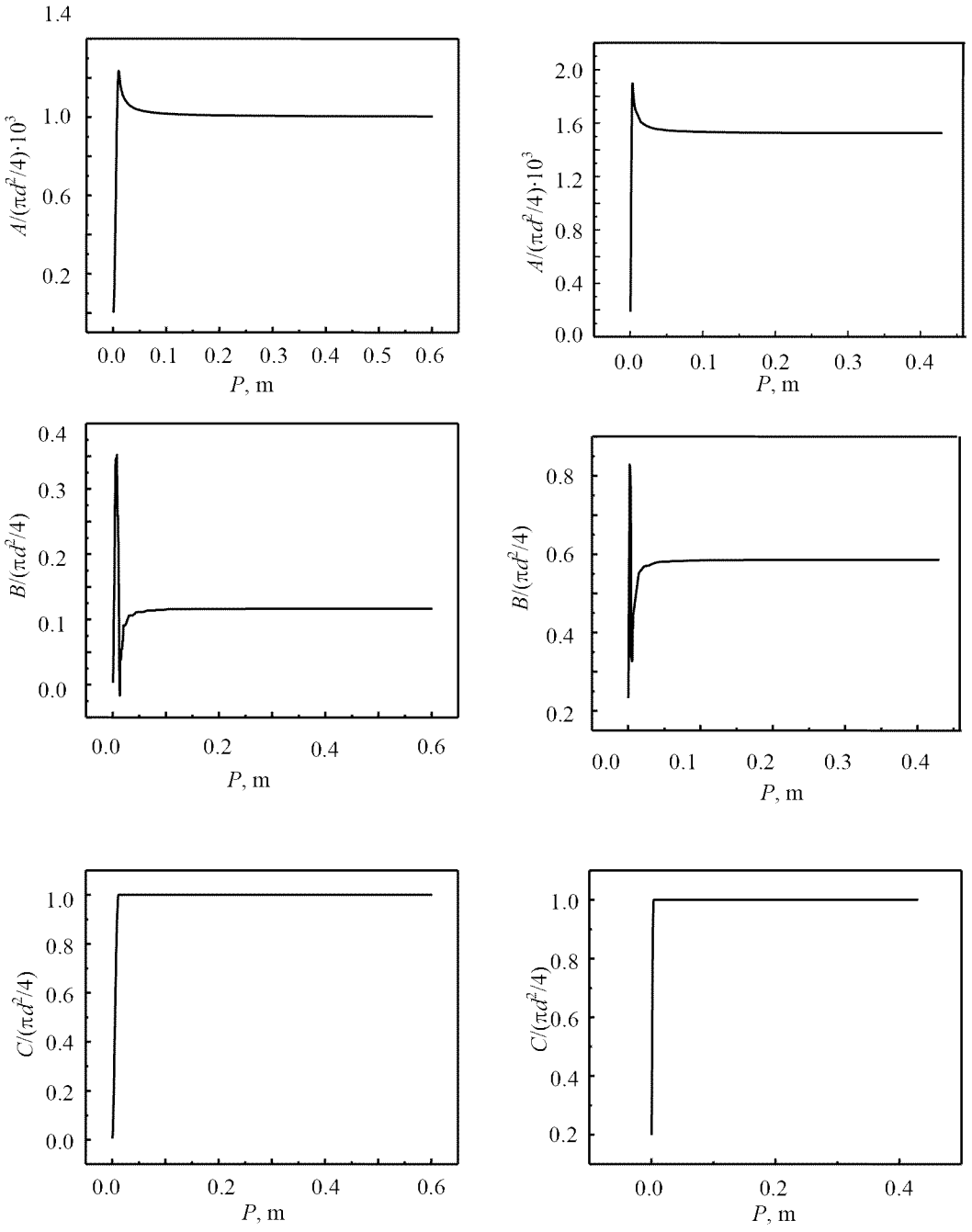

(a) (b)

Fig. 8 Dependence of A, B, C coefficients in equation (11) on penetration depth P.
(a) ogival head, (b) spherical head

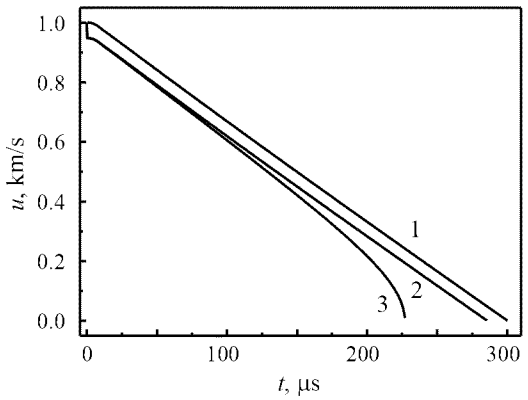

Fig. 9 Difference in dependence of penetration velocity u vs. time t for ogival head at impact velocity U_s= 1.0 km/s for rigid (1), quasi-rigid projectile (2), and with account for forced elastic oscillations (3). Projectile — steel T-200, target — Al 7071-T651

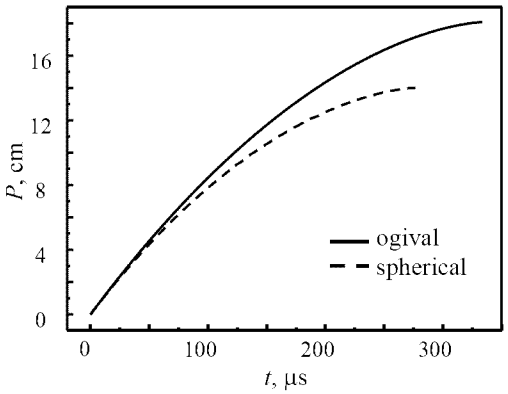

Fig. 10 Dependence of penetration depth P vs. time t

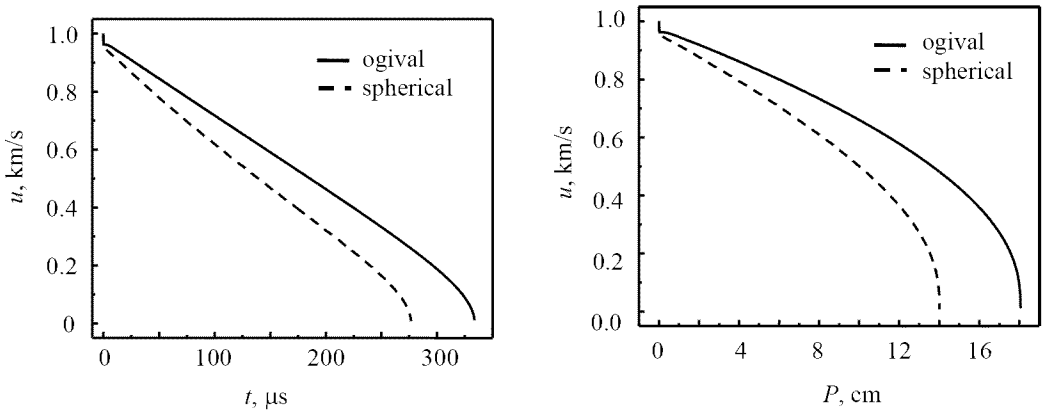

Fig. 11 Dependence of penetration velocity u vs. time t and penetration depth P

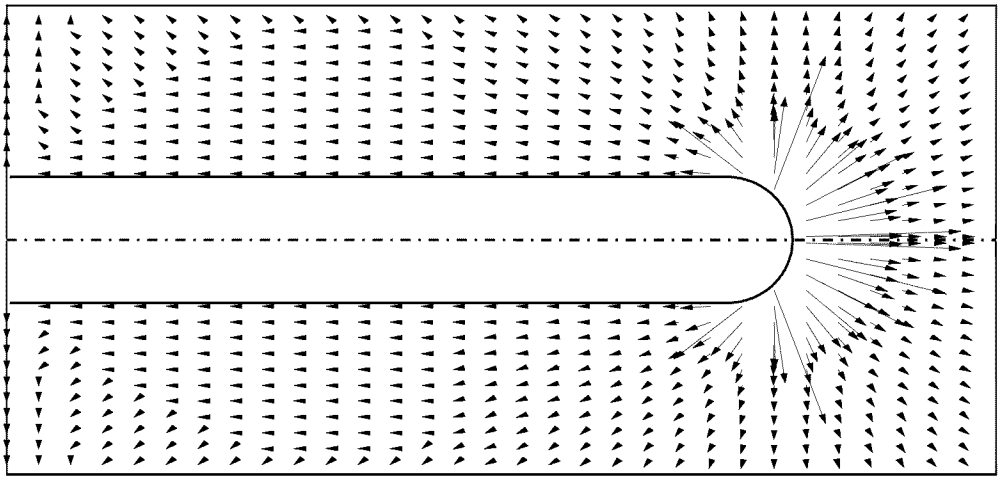

Fig. 12 Velocity fields near the projectile. Spherical head

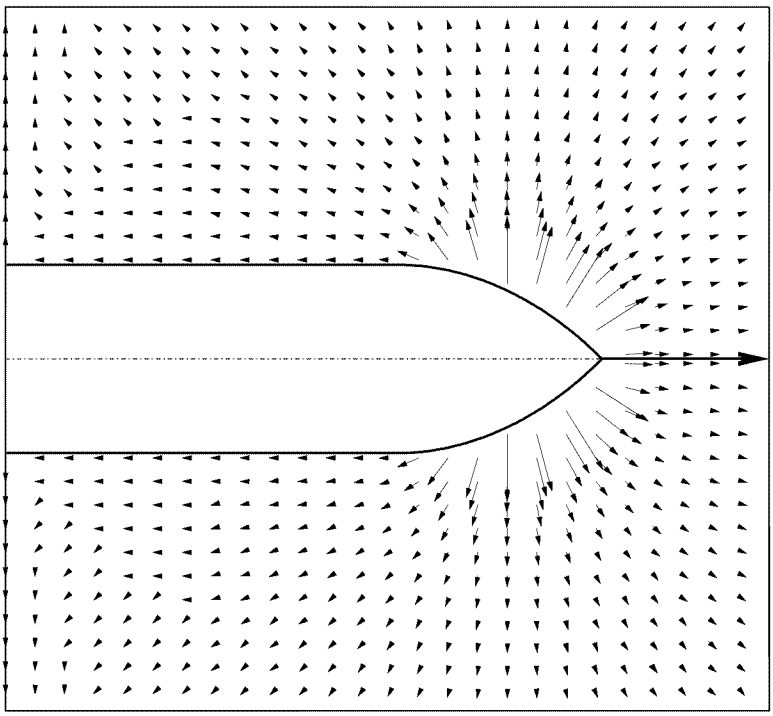

Fig. 13 Velocity fields near the projectile. Ogival head.

Calculations by the model were compared with available experimental data. Fig. 14 presents penetration depth dependence on impact velocity for projectile with spherical nose. Target material — aluminium 6061-T651, Y= 400 MPa, E= 68.9 GPa, ν= 0.33, ρ = 2710 kg/m^3, projectile — steel, ρ_p= 8000 kg/m^3, E_p = 210 GPa, ν_p= 0.29,. L= 74.7 mm, a= 3.55 mm. The plots in Fig. 15 demonstrate penetration depth dependence on impact velocity for projectiles with ogival nose. Target material in Fig. 15 (a) — aluminium 6061-T651, Y= 400 MPa, E= 68.9 GPa, ν= 0.33, ρ = 2710 kg/m^3, projectile — steel T-200, ρ_p= 8020 kg/m^3, E_p = 210 GPa, ν_p= 0.29, L= 82.9 mm, a= 3.55 mm. Target material in Fig. 15 (b) — aluminium 7075-T651, Y= 448 MPa, E= 73.1 GPa, ν= 0.33, ρ = 2710 kg/m^3, projectile — steel T-200, ρ_p= 8020 kg/m^3, E_p = 210 GPa, ν_p= 0.29, L= 82.91 mm, a= 3.55 mm. Target resistance R_t for calculations in Fig. 14, 15 was evaluated by formula (16). These figures illustrate noticeable influence of projectile forced elastic oscillations on penetration depth.

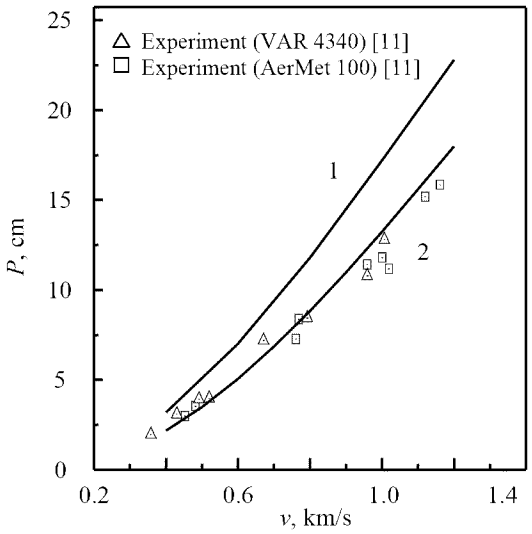

Fig. 14 Dependence of calculated penetration depth on impact velocity (spherical nose): 1 – rigid projectile, 2 – elastic projectile. Experimental points borrowed from [11]

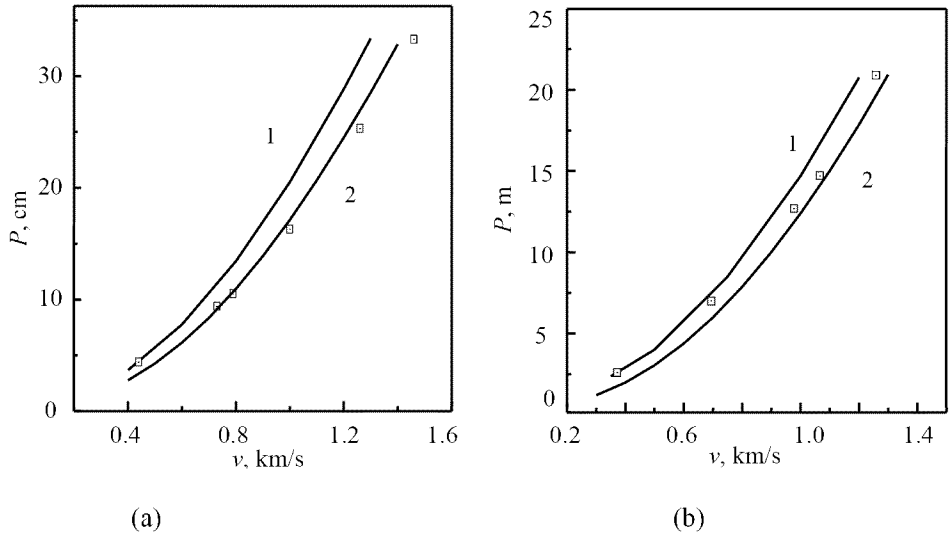

Fig. 15 Dependence of calculated penetration depth on impact velocity (ogival nose): 1 – rigid projectile, 2 – elastic projectile. Experimental points were taken from: a) [7]; b) [8]

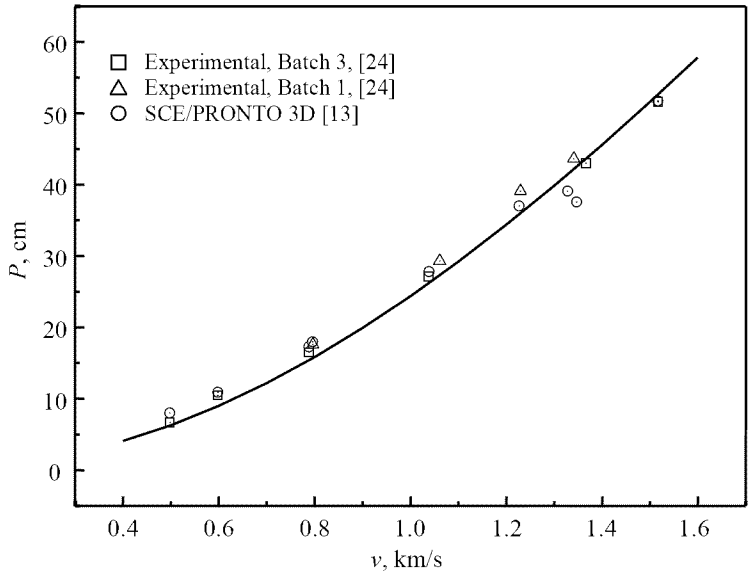

Fig. 16 Dependence of calculated penetration depth on impact velocity (ogival nose). Target material — limestone, a projectile — steel 4340. Experimental and initial data for calculation are taken from [13]

Fig. 16 shows comparison of model predictions with experimental data for limestone. Target resistance R_t was calculated by (19), ρ = 2310 kg/m^3, projectile — steel 4340, ρ_p= 7850 kg/m^3, E_p = 210 GPa, ν_p= 0.29,. L= 71.0 mm, a= 3.55 mm.

Results of comparison with experimental data show reasonably good correspondence. Still there is need for future investigation of oscillation on penetration for different pairs of projectile-target both theoretical and experimental. The existence of publications where good agreement of theoretical predictions and experimental data was reached without involvement of oscillation phenomena (see e.g. Yarin [16]) may be an indication that a combination of factors — from difference in formulations of initial problem to improper account of different factors and their interaction — can be the cause (and the subject of further analysis).

5. Conclusion

New ballistic equation of normal friction-free penetration in semi-infinite targets of non-deformable axisymmetric projectiles of various shapes has been proposed and analyzed. It has a simple and clear mechanical structure and is built on the base of Lagrange-Cauchy integral for non-stationary irrotational motion of ideal fluid. The equation can be used for analysis of penetration in elastic-plastic and elastic-brittle materials.

The equation of projectile motion is constructed on the base of definition of integral force of resistance acting on projectile from the part of target. Its value is determined by surface integrals from the functions of velocities potential for target material on the projectile surface.

The suggested ballistics equation allows to make a fast and rather reliable prediction of integral characteristics of normal penetration of projectiles in target (penetration depth, drag force acting on projectile and its components, penetration velocity) without additional fitting parameters.

A number of calculations were carried out for long steel projectiles of different shapes penetrating aluminum targets at velocities in the range of 600–1600 km/s. The results were compared with available experimental and computed data [7-9,11,13]. A comparison of theoretical curve penetration depth – impact velocity with experimental data shows that the experimental data are lower than the theoretical curve for rigid projectiles. The models proposed in works [7-9,11,12] show a similar trend, and these deviations have a systematic nature. In this connection we took into account forced elastic longitudinal oscillations of projectile, caused by sudden application of braking force. The existence of such oscillations was observed in recent experiments by Frew, Forrestal, Cargile [31] and also in much earlier research by Masket, (1949) [32] and Bluhm (1956) mentioned by Goldsmith [28, chapter 6]. The energy of these oscillations caused by drag force (work of drag force spent on elastic oscillations) is accumulated and has maximum in the end of penetration though deformations of penetrator are elastic (small). It is shown that these elastic oscillations noticeably affect the final depth and velocity of penetration. In our opinion longitudinal oscillations can also reduce tangential stresses on the surface of projectile thus minimizing friction forces. A comparison of final penetration depths with the experimental data is in a good agreement. A critical impact velocity is defined at which projectile undergoes plastic deformations and loses its shape and stability of motion. The obtained estimate for a critical

impact velocity has obvious mechanical meaning and generalizes a well known estimate for critical velocity of longitudinal impact of rigid mass on a rod.

Appendix

Example estimate of dynamic yield stress

The projectile with a spherical nose made from steel VAR 4340 has the following parameters $E_p = 210$ GPa, $\rho_p = 8000$ kg/m^3, $L = 74.675 \cdot 10^{-3}$ m, $d = 7.11 \cdot 10^{-3}$ m, $\overline{A} = 1.5 \cdot 10^{-3}$, $\overline{B} = 0.58$, $\overline{C} = 1.00$, and the target made of aluminium alloy 6061-T651 has the following properties

$\rho = 2710$ kg/m^3, $E_p = 68.9$ GPa, $\nu = 0.33$, $Y = 400$ MPa.

From the experiment $U_{sC} \approx 1000$ ms^{-1} (see [9]) and

$$\overline{Y}_p = \left(1 + \frac{2.71 \cdot 1.5}{8 \cdot 74.675}\right) \cdot Y_p = (1 + 0.0068) \cdot Y_p = 1.0068 Y_p \ \text{GPa},$$

$$R_t = \frac{2Y}{3}\left\{1 + \ln\left[\frac{E}{3(1-\nu)Y}\right]\right\} = \frac{2 \cdot 400}{3}\left\{1 + \ln\frac{689}{8}\right\} = 1455 \ \text{GPa},$$

$$\overline{R}_t = 1.0 \cdot 1455 = 1455 \ \text{GPa}, \quad c_0 = \sqrt{\frac{210 \cdot 10^9}{8 \cdot 10^3}} = 5123 \ \text{ms}^{-1},$$

and from equation

$$U_{sC} = \frac{Y_p \cdot 10^{-3}}{210} \cdot 5123 + \sqrt{\frac{2 \cdot 10^6}{2.71 \cdot 10^3 \cdot 0.58}\left(1.0068 Y_p - 1455\right)} = 1000 \ \text{ms}^{-1},$$

we find $Y_p = 2135$ GPa. Quasi-static yield stress is $Y_{ps} = 1481$ MPa (see [8]) and ratio $\frac{Y_p}{Y_{ps}} = \frac{2135}{1481} = 1.44$, which is a rather good result.

II Development of new numerical-analytical model of expansion of spherical cavity in brittle material on the basis of modern concepts of mechanics of compressible porous and powder materials

Introduction

It is well known that the models of mechanics of expansion of spherical and cylindrical cavities in materials have essential significance for investigation of high-velocity penetration in these materials. Both models were used for penetration problems. However, it is noted that generally model of expansion of spherical cavity better describes high-velocity penetration. Sufficiently complete review and detailed analysis of existing models of cavity expansion in different materials can be found in [33]. Notwithstanding considerable achievements in construction of such models it is noted in [33] that sufficiently simple and adequate analytical models of cavity expansion in brittle materials are still in demand. Most widespread is the model proposed in [23,33]. In this model for the material in comminuted or pulverized region was used Mohr-Coulomb law (with or without shear saturation) which defines the correspondence between compressive and shearing stresses in this region using coefficient of internal friction. Cavity expansion pressure essentially depends upon this coefficient [23,34]. This means that material properties in comminuted region strongly influence the penetration resistance and play important role in its definition. To estimate this friction coefficient fitting experiment is used (in particular, normal impact of sphere on sample [34]), which essentially complicates the application of the model [23,33]. The new model of spherical cavity expansion in brittle material uses for comminuted region material and its boundary with cracked region rheological models of porous and compressible powder materials based on approaches developed in [35-38]. This allows to exclude friction coefficient which is determined in complex experiment. Instead, new parameter, in our opinion, more naturally calculated parameter is introduced: porosity of fractured initial material. Herein lies the main difference of the proposed model from existing ones.

1. Main equations of the model

Figure 1 presents geometrical scheme of the proposed model of expansion of spherical cavity. According to this scheme three regions with different stress-strain state are formed in the material: 1) r > c —

elastic region; 2) b < r < c — dilatation pore formation region; a < r < b — pulverized region. Let's consequentially consider these regions.

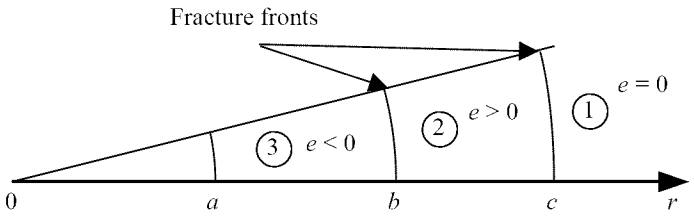

Fig. 1 Scheme of the model of cavity expansion in spherical coordinates 0rφθ:
1 — elastic region (r > c, volume deformation e = 0); 2 — dilatation and pore formation region (b < r < c, volume deformation > 0); 3 — fractured material (a < r < b, volume deformation e < 0).

1.1. Elastic region, r ≥ c.

In spherical coordinates 0rφθ stress-strain state in this region is determined by the following equations [38]:

$$\frac{d\sigma_r}{dr} + 2\frac{\sigma_r - \sigma_\varphi}{r} = 0, \text{ (equilibrity equation)} \tag{1}$$

$$e_r = \frac{du}{dr},\ e_\varphi = e_\theta = \frac{u}{r} \text{ (strain-displacement relations)} \tag{2}$$

$$e_r = \frac{1}{E}\left[\sigma_r - 2\nu\sigma_\varphi\right],\ e_\varphi = e_\theta = \frac{1}{E}\left[(1-\nu)\sigma_\varphi - \nu\sigma_r\right], \text{ (Hook's law)} \tag{3}$$

with boundary conditions:

$$u(\infty) = 0;\ \sigma_\varphi(r = c) = \sigma_\theta(r = c) = \sigma_f \tag{4}$$

where E, ν — Young's modulus and Poisson ratio respectively, σ_f — material strength in uniaxial tension.

Solving equations (1)—(4) we obtain

$$u = \frac{1+\nu}{E}\sigma_f\frac{c^3}{r^2},\ \sigma_r = -2\sigma_f\left(\frac{c}{r}\right)^3,\ \sigma_\varphi = \sigma_f\left(\frac{c}{r}\right)^3,\ r \ge c, \tag{5}$$

and for radial displacement $u(c)$ we have

$$u(c) = \frac{1+\nu}{E}\sigma_f c. \tag{6}$$

From (5) follows that in the elastic region hydrostatic pressure $p = -(\sigma_r + \sigma_\varphi)/3 = 0$, and volume deformation $e = e_r + 2e_\varphi = 0$.

1.2. Dilatation and pore formation region, $b \le r \le c$.

Cracked and dilated material in this region is formed at the boundary $r = c$ from elastic region $r > c$ where tensile hoop stresses $\sigma_\varphi = \sigma_\theta$ reach material strength at uniaxial tension σ_f, i. e. boundary $r = c$ is considered as a fracture front of elastic region and front of transition of material into a state with different mechanical properties. Cracking and dilatation is accompanied by pore formation. Thus, elastic region $r \ge c$ is bounded by dilatation and pore formation region $b \le r \le c$ where radial cracks are assumed to be distributed so that hoop stresses in the whole region are equal to zero, i. e. $\sigma_\varphi = \sigma_\theta = 0$. Because of this material in the region $b \le r \le c$ is considered as a continuum elastically deformable in radial direction with uniaxial (radial) stress state with fracture occurring at the boundary $r = b$ where stress-strain state of material satisfies fracture criterion and material changes state stepwise.

At the boundary $r = b$ stresses in dilatation pore formation region satisfy the following boundary conditions

$$\sigma_r(r = b + 0) = \sigma^*,\ \sigma_\varphi(r = b + 0) = \sigma_\theta(r = b + 0), \tag{7}$$

where σ_r — radial stresses, σ_φ, σ_θ — hoop stresses, σ^* — stress defined below (see (21), (22)) from fracture criterion at the front $r = b$.

At the boundary $r = c$ stresses in this region are equal

$$\sigma_r(r = c - 0) = -2\sigma_f,\ \sigma_\varphi(r = c - 0) = \sigma_\theta(r = c - 0). \quad (8)$$

At crossing boundary r = c stresses σr are continuous and stresses σφ, συ are discontinuous.

Thus, stress-strain state in dilatation and pore formation region is defined by equations [9,10]

$$\frac{d\sigma_r}{dr} + 2\frac{\sigma_r}{r} = 0, \quad (9)$$

$$\sigma_r = \frac{du}{dr} \quad (10)$$

with boundary conditions (7) for equation (9) and boundary condition (6) for equation (10). Integrating (9), (10) we have

$$\sigma_r = \sigma^*\left(\frac{b}{r}\right)^2, \quad (11)$$

$$u = -\frac{\sigma^*}{E}b\left(\frac{b}{r} - \frac{b}{c}\right) + \frac{\sigma_f(1+\nu)}{E}c, \quad (12)$$

where $u = u(r)$ — radial displacements of material during deformation ($u(r)$ — continuous function of argument r).

From (8), (10) and (12) taking into account continuity of radial stresses at $r = c$ we find position of fracture front

$$c = b\sqrt{\frac{\left(-\sigma^*\right)}{2\sigma_f}}. \quad (13)$$

From (13) follows that dilatation and pore formation region exists for materials ($c > b$) that satisfy condition $2\sigma_f < (-\sigma^*)$. This condition is further assumed satisfied.

From this and from (12) for displacement u of boundary $r = b$ and deformations in the considered region at $r = b + 0$ we have

$$u = -\frac{\sigma^*}{E}b\left(1 - \frac{(1-\nu)}{2}\sqrt{\frac{2\sigma_f}{HM}}\right), \quad (14)$$

$$e_r = \frac{du}{dr} = \frac{\sigma^*}{E} < 0;\ e_\varphi = \frac{u}{b} = -\frac{\sigma^*}{E}\left(1 - \frac{(1-\nu)}{2}\sqrt{\frac{2\sigma_f}{\left(-\sigma^*\right)}}\right) > 0,$$

$$e_c = e_r + 2e_\varphi = -\frac{\sigma^*}{E}\left(1 - (1-\nu)\sqrt{\frac{2\sigma_f}{\left(\sigma^*\right)}}\right) > 0,$$

$$\gamma_c = \sqrt{\frac{2}{3}}\left|e_r - e_\varphi\right| = -\sqrt{\frac{2}{3}}\frac{\sigma^*}{E}\left(2 - \frac{(1-\nu)}{2}\sqrt{\frac{2\sigma_f}{\left(-\sigma^*\right)}}\right),$$

where e_r — radial deformation; $e_\varphi = e_\theta$ — hoop deformations; e_c — volume deformation, and γ_c — intensity of shear deformations at $r = b + 0$.

Because material cracking leads to pore formation and volume deformation rate $\dot{e}$ is related to porosity change rate $\dot{\theta}$ by differential dependence

$$\dot{e} = \frac{\dot{\theta}}{1-\theta},$$

or

$$de = \frac{d\theta}{1-\theta}, \quad (15)$$

then material porosity θ in the dilatation region at $r = b + 0$ which was formed in this material after its fracturing can be found from the integral of equation (15)

$$e = \ln\frac{1-\theta_0}{1-\theta}, \quad (16)$$

at $e = e_c$; θ_0 — initial (before deformation) porosity of material in the region ($b < r < c$).

Thus, from (16) at $e = e_c$ for "full" porosity θ^* of material at $r = b + 0$ we have

$$\theta^* = 1 - (1 - \theta_0)\exp(-e_c). \quad (17)$$

From here (at $\theta_0 = 0$) for "induced" porosity of material θ_c (i. e. additional to θ_0 porosity formed during material cracking in the region $b < r < c$) we have

$$\theta_c = 1 - \exp(-e_c). \quad (18)$$

1.3. Pulverized region (a < r < b)

Region ($a < r < b$) consists from compressed fractured material formed from cracked material of region ($b < r < c$) at the front $r = b$ where material is comminuted (fragmented) by shearing stresses and then densified. Because of this we can use for the material of pulverized region rheological models of compactable porous and powder materials.

Further for such materials we use the following constitutive equations [35-38]

$$\begin{cases} \dfrac{p^2}{\psi} + \dfrac{\tau^2}{\varphi} = \dfrac{2}{3}(1-\theta)Y_s, \\ \varphi p = s\psi\tau \end{cases} \quad (19)$$

where $\psi = \dfrac{2}{3}\dfrac{(1-\theta)^3}{\theta}$, $\varphi = (1-\theta)^2$ — functions of porosity θ; $s = \dfrac{\dot{e}}{\dot{\gamma}}$ — index of deformation state depending on velocities of volume $\dot{e}$ and shearing $\dot{\gamma}$ deformations; $p = \dfrac{\sigma_1 + \sigma_2 + \sigma_3}{3}$, σ_1, σ_2, σ_3 — main stresses, $\tau = \dfrac{1}{\sqrt{3}}\left[(\sigma_1 - \sigma_2)^2 + (\sigma_2 - \sigma_3)^2 + (\sigma_1 - \sigma_3)^2\right]^{1/2}$; Y_s — flow stress of solid phase at uniaxial compression. First equation in (19) is a condition of flow of porous body (in the space of variables $p - \tau$ it describes flow ellipse), second equation in (19) is an associated flow law.

At the front $r = b$ (see Fig. 1) first equation in (19) we consider as a condition of fracturing (comminution) by shearing stresses of a material in the region 2 with the porosity $\theta = \theta^* = 1 - (1 - \theta_0)\exp(-e_c)$, see (17). Second — as an associated law of fracturing (compaction) of material in the region 2 with "induced" porosity $\theta_c = 1 - \exp(-e_c)$, see (18) (i. e. porosity formed by radial cracks in region 2 and additional to initial porosity θ_0). Here Y_s is strength limit at uniaxial compression of porous free material. Thus, fracturing and densification of the material in region 2 at the front $r = b$ (i. e. formation of material of region 3) we consider as "quasi-plasticity" of porous material.

Let's define the value of deformation state index s at the front $r = b$. At this front it can be written out in the form

$$s = \frac{\dot{e}}{\dot{\gamma}} = \frac{de}{d\gamma} = \frac{e^+ - e^-}{\gamma^+ - \gamma^-}, \quad (20)$$

where $e = e_r + 2e_\varphi$, $\gamma = \sqrt{\dfrac{2}{3}}\left|e_r - e_\varphi\right|$, $e_r = \dfrac{du}{dr}$, $e_\varphi = \dfrac{u}{r}$ — radial and tangential components of deformation, signs "+", "–" denote values before front (at $r = b + 0$) and behind the front (at $r = b - 0$), respectively. If we take into account that $e_r < 0$, $e_\varphi > 0$, $e_\varphi^+ = e_\varphi^-$, and $e_r = e - 2e_\varphi$, then from (20) we obtain

$$s = \frac{e^+ - e^-}{\gamma^+ - \gamma^-} = \sqrt{\frac{3}{2}}\frac{e^+ - e^-}{\left|e_r^+ - e_\varphi^+\right| - \left|e_r^- - e_\varphi^-\right|} = \sqrt{\frac{3}{2}}\frac{e^+ - e^-}{-e_r^+ + e_\varphi^+ + e_r^- - e_\varphi^-} = \sqrt{\frac{3}{2}}\frac{e^+ - e^-}{-e_r^+ + e_r^-} = \sqrt{\frac{3}{2}}\frac{e^+ - e^-}{-e^+ + e^-} = -\sqrt{\frac{3}{2}}.$$

This value of index $s = -\sqrt{\dfrac{3}{2}}$ corresponds to compression in the die mold, spherical in this case.

If in relationships (19) we put $\theta = \theta^*$, $p = \dfrac{\sigma_r + 2\sigma_\varphi}{3}$, $\tau = \sqrt{\dfrac{2}{3}}\left|\sigma_r - \sigma_\varphi\right|$, $\sigma_r = \sigma^*$, $s = -\sqrt{\dfrac{3}{2}}$ (i. e. consider conditions (19) at the front $r = b$) and exclude σ_φ from them, we obtain the following equation for determination of radial stress $\sigma_r = \sigma^* < 0$ at the front $r = b$

$$\sigma^* = -CY_s, \; C = \frac{2\left(1-\theta^*\right)^{3/2}}{3\sqrt{\theta^*}}, \quad (21)$$

where porosity θ^* is calculated by formulas (see 14),(17)).

$$\theta^* = 1-(1-\theta_0)\exp(-e_c),\ e_c = -\frac{\sigma^*}{E}\left[1-(1-\nu)\sqrt{\frac{2\sigma_f}{(-\sigma^*)}}\right] > 0$$

It is obvious that stress $\sigma^* < 0$ depends only on material properties and thus is its characteristics.

Nonlinear equation (21) can be solved by method of consequent approximations

$$\sigma^*_{n+1} = -\frac{2(1-\theta^*_n)^{3/2}}{3\sqrt{\theta^*_n}}Y_s,\ \theta^*_n = 1-(1-\theta_0)\exp\left(\frac{\sigma^*_n}{E}\left[1-(1-\nu)\sqrt{\frac{2\sigma_f}{(-\sigma^*_n)}}\right]\right),\ \sigma^*_0 = Y_s,\ n = 0,1,2,\ldots. \quad (22)$$

It should be noted that dimensions of regions 2 and 3 (see (13) and Fig. 1) are connected by relationship

$$\frac{b}{c}\sqrt{\frac{2\sigma_f}{(-\sigma^*)}} \le 1,$$

Further we assume that in the region ($a < r < b$) porosity θ_k and volume deformation e_k are constant (do not depend on r) and also $\dot\theta_k = \dot e_k = 0$ during cavity expansion. Such material state in the region ($a < r < b$) takes place at the fracture front $r = b$ (see Fig. 1). It means that at the level of stress $\sigma_r = \sigma^*$ material in the region ($b < r < c$) at the boundary $r = b$ fractures by shearing stresses, volume deformation and porosity of fractured material in the result of densification reach maximum values e_k, $\theta_k << 1$. After that the material becomes porous incompressible medium which behaves in accordance with constitutive equations (19) at $s = -\sqrt{\frac{3}{2}}$ (compression in spherical die mold) and $\theta = \theta_k$. Because of this from second equation in (19) we have

$$\tau = -\sqrt{\frac{3}{2}}\frac{\theta_k}{1-\theta_k}p,$$

where hydrostatic pressure $p = \frac{\sigma_r + 2\sigma_\varphi}{3}$ and intensity of shearing stresses $\tau = \sqrt{\frac{2}{3}}|\sigma_r - \sigma_\varphi|$. From this we have

$$\sigma_\varphi = \left(1-\frac{3}{2}\theta_k\right)\sigma_r,\ \sigma_r - \sigma_\varphi = \frac{3}{2}\theta_k\sigma_r. \quad (23)$$

At the boundary $r = b$ takes place pressure and shearing stress discontinuity: hydrostatic pressure increases ($p(r=b+0) = \frac{\sigma^*}{3}$, $p(r=b-0) = \sigma^*$), and intensity of shearing stresses decreases ($\tau(r=b+0) = \sqrt{\frac{3}{2}}|\sigma^*|$, $\tau(r=b-0) = \sqrt{\frac{3}{2}}|\sigma^*|\theta_k$).

In accordance with (23) equilibrium equation in the region ($a < r < b$) takes form

$$\frac{d\sigma_r}{dr} + 2\alpha\frac{\sigma_r}{r} = 0,\ \alpha = \frac{3}{2}\theta_k,\ \sigma_r(r=b) = \sigma^*,$$

and its solution is function

$$\sigma_r = \sigma^*\left(\frac{b}{r}\right)^{2\alpha}. \quad (24)$$

Thus, during cavity expansion (i. e. with increasing radius a) region ($a < r < b$) is joined at the boundary $r = b$ by fractured and densified material with porosity θ_k.

Let's now estimate volume deformation e_k and porosity θ_k of the material in the region ($a < r < b$). This estimate will be done taking into account elastic compressibility of material of solid phase. Let's note that conditions (19) do not presuppose compressibility of the solid phase, hence compressibility of the medium with rheology (19) takes place due to porosity [35-38].

On the basis of accepted assumptions, continuity equations in the region ($a < r < b$) have the form

$$\frac{\partial\dot u}{\partial r} + 2\frac{\dot u}{r} = 0 \quad (25)$$

where for convenience it is accepted $t \equiv b$, and from continuity of displacements at the front $r = b$ for the velocity $\dot u = v^*$ of the boundary $r = b$ from (12) we have expression

$$v^* = \dot{u}(b) = \frac{du}{db} = -\frac{\sigma^*}{E}\left(1 - \sqrt{\frac{2\sigma_f}{(-\sigma^*)}}\right) + \frac{\sigma_f(1+\nu)}{E}\sqrt{\frac{-\sigma^*}{2\sigma_f}}. \qquad (26)$$

From this we have the following solution of equation (25)

$$\dot{u} = v^*\left(\frac{b}{r}\right)^2. \qquad (27)$$

Let's define now the relationship between average volume deformation e_k in the region ($a < r < b$) and ratio $\frac{b}{a}$. By definition

$$e_k = -\frac{\delta v}{v},$$

where $\delta v = \frac{4}{3}\pi a^3$ — volume of spherical cavity; $v = \frac{4}{3}\pi(b-u)^3$ — initial volume of the region ($a < r < b$); $u = be_\varphi$, $e_\varphi^* = -\frac{\sigma^*}{E}\left(1 - \frac{1-\nu}{2}\sqrt{\frac{2\sigma_f}{(-\sigma^*)}}\right)$ — elastic displacement of the boundary $r = b$. As a result we have relationship

$$e_k = -\frac{1}{\left(1-e_\varphi^*\right)^3}\left(\frac{a}{b}\right)^3,\ e_\varphi^* = -\frac{\sigma^*}{E}\left(1 - \frac{1-\nu}{2}\sqrt{\frac{2\sigma_f}{(-\sigma^*)}}\right), \qquad (28)$$

from which it follows that ratio $\frac{a}{b}$ remains constant during cavity expansion

$$\frac{a}{b} = \left(1-e_\varphi^*\right)(-e_k)^{1/3}.$$

From this and from (27) for velocity of cavity expansion $\dot{u}(a) = \frac{da}{db}$ we obtain

$$\frac{da}{db} = \frac{v^*}{\left(1-e_\varphi^*\right)^2(-e_k)^{2/3}} = const,$$

and

$$\frac{a}{b} = \frac{v^*}{\left(1-e_\varphi^*\right)^2(-e_k)^{2/3}} \qquad (29)$$

at cavity expansion from zero radius. This relation and formula (28) define volume deformation e_k in the region ($a < r < b$)

$$e_k = \frac{v^*}{\left(1-e_\varphi^*\right)^3}. \qquad (30)$$

Note: If we use true deformation, then instead of formulas (28)-(30) we have, respectively, formulas

$$e_k = -\left(\frac{a}{b}\right)^3\frac{1}{1-(a/b)^3},\ \frac{a}{b} = v^{*1/3},\ e_k = -\frac{v^*}{1-v^*}.$$

Porosity θ_k we find from differential equation

$$de = \frac{d\theta}{1-\theta}$$

with initial condition $e = e_c$ at $\theta = \theta^*$. This equation describes change of volume deformation e that is caused by change only of porosity θ. Its solution is function

$$\theta = 1 - (1-\theta^*)\exp(e_c - e),$$

and for desired porosity we have formula

$$\theta = 1 - (1-\theta^*)\exp(e_c - e_k + e_{ks}), \qquad (31)$$

where e_{ks} — volume average deformation in the region ($a < r < b$) caused by elastic deformation of solid phase. The account of e_{ks} is necessary because deformation e_k defined by formula (30) is a sum of e_{ks} and volume deformation $e_p = (e_k - e_{ks})$ of pore compression.

The value of e_{ks} can be estimated by formula

$$e_{ks} = \frac{\sigma^*}{K_s}, \tag{32}$$

where $K_s = \frac{E_s}{3(1-2\nu_s)}$ — modulus of volume compression of solid phase (i. e. porousless material). Thus, porosity θ_k is defined by formula

$$\theta = 1 - (1 - \theta^*)\exp(e_c - e_k + e_{ks}), \tag{33}$$

where $e_{ks} = \frac{\sigma^*}{K_s}$.

In the case of small values of θ_k, e_k, e_c, e_{ks} formula (33) takes more simple form

$$\theta_k = \theta^* - e_c + e_k - e_{ks},\ e_{ks} = \frac{3(1-\nu_s)}{E_s}\sigma^*,$$

Finally, from (24) for pressure R_t in the cavity we have

$$R_t = -\sigma^*\left(\frac{b}{a}\right)^{2\alpha}, \tag{34}$$

where σ^* is determined by formulas (21).

Example

Ceramics AD995 [1]: E = 373.14 GPa, K = 231.8 GPa, σ_f = 0.262 GPa, ν = 0.232, Y_s = 2.26 GPa. Equation (21) is solved by method of simple iteration (22):

$$\sigma^*_{n+1} = -\frac{2\left(1-\theta^*_n\right)^{3/2}}{3\sqrt{\theta^*_n}}Y_s,\ \theta^*_n = 1-(1-\theta_0)\exp\left(-e_c^{(n)}\right),\ e_c^{(n)} = -\frac{\sigma^*_n}{E}\left[1-(1-\nu)\sqrt{\frac{2\sigma_f}{\left(-\sigma^*_n\right)}}\right],$$

$$\sigma^*_0 = Y_s,\ n = 0,1,2,\ldots.$$

In the result we have the following figures for desired values:

$\sigma^* = -10.9$ GPa, $e_c = 0.024$, $\theta^* = 0.024$, $C = 4.15$, $v^* = 0{,}027$, $\frac{a}{b} = 0.299$, $e_{ks} \approx -0.047$, $\theta_k \approx 0.018$,

$$e_k = -0.029.$$

For the pressure in the cavity we obtain

$$R_t = 10.9\left(\frac{1}{0.299}\right)^{3\cdot 0.018} = 11.63 \text{ GPa}.$$

This value is close to values 7 — 9 GPa found in literature.

III. Investigation of deformation process at high-speed loadings of ceramic materials with diamond-like structure in adiabatic approach at microlevel

Introduction

This problem can be solved by means of a method of pseudo-potentials as it was shown in previous works (by the example of calculation of different physical values). In terms of this method a solution of the problem can be presented as follows.

1. Calculation of pseudo-potential for separate components of a material, if a material is multicomponent.
2. Construction of a complete pseudo-potential in view of materials structure.
3. Calculation of total energy of electron-ion system in terms of perturbation theory provided that matrix elements of pseudo-potential of atoms are small in comparison with Fermi's energy.
4. Stress appearing in a material at any loading is commonly defined by the first derivative of total energy on deformation.

Investigation of one axis deformation along axis c in titanium by means of interlayer interaction showed that densely packed basic, atomic planes are easily elongated or compressed relatively each other. While considering ideal structures, the basic planes remain parallel at one axis deformations, only distances among those vary.

Results of investigation of process high-speed loading (one axis) of titanium were used as an intermediate stage for transition to ceramic materials with diamond-like structure. We described these materials in hexagonal axes that enabled to allocate parallel densely packed atomic planes.

As a result of carried out numerical experiment it was obtained that densely packed atomic planes at high-speed one axis loadings are deformed in different ways (depending on their distance from each other and relative positioning of atoms on these planes).

The developed technique is applied for nanoparticles of diamond-like ceramics.

1. Calculation of mechanical characteristics of diamond-like materials, proceeding from energy of interaction of atomic planes

Investigation of a course of physical processes (deformation, fracture) in materials between micro - and macro - scales remains an actual and unresolved problem of physical modeling in materials science [39].

Fracture process of brittle materials is structural - multilevel, and its adequate modeling is associated with a necessity of attraction as theoretical methods and modern experimental and computer facilities [40]. Theoretical methods which were applied to a problem of deformation and fracture of a wide class of materials, originate from the work of Barrenblat [41] for quasi-brittle solid bodies (a model of cohesion zone). In terms of continual theory the nonlinear law of boning of force and displacement for atoms in top of a crack is postulated. One of the basic assumptions lying in a background of all models of cohesion zone is associated with a kind of distribution of cohesion forces.

In terms of continual theory the exact form of this distribution is unknown, but some data can be obtained from experimental works on investigation of fracture in the field of interfaces.

This effort is to find out, being based on the method of pseudo-potentials, the mechanism of fracture at microlevel with macroscopic mechanical characteristics (diamond-like materials) at one axis tension and compression.

For a description of fracture process of diamond-like materials (diamond SiC, AlN and BN) at one axis loading we use a value of energy of interaction between atomic planes (perpendicular to axis of loading). It essentially differs from standard approach where for calculation of mechanical characteristics on microlevel a full energy per atom in a material is used [42-45], i.e. on averaging on the whole volume, that is not adequate to a local character of crack origin.

Due to anisotropy of single crystal under the influence of loadings, a material is more easy deformed on certain crystallographic directions [44-45]. For investigated materials with cubic structure these directions are body diagonals of elementary cell. Atomic planes, perpendicular to diagonals, are densely packed. Therefore it is expedient to describe structure of diamond-like materials in hexagonal axes, having chosen for an axis a spatial diagonal of cube [111]. Thus the planes {111}, being the planes of octahedron, would have the indexes 001 (i.e. they are the basic planes).

Structure of diamond and diamond-like materials would be described in this case by three-layer alternation of planes (001) like $AA'BB'CC'$ where layers (planes) A, B, C consist of atoms of one grade (C, B, Al, Si), and layers (planes) A', B', C' - from atoms of other grade (C, N) (see fig. 1).

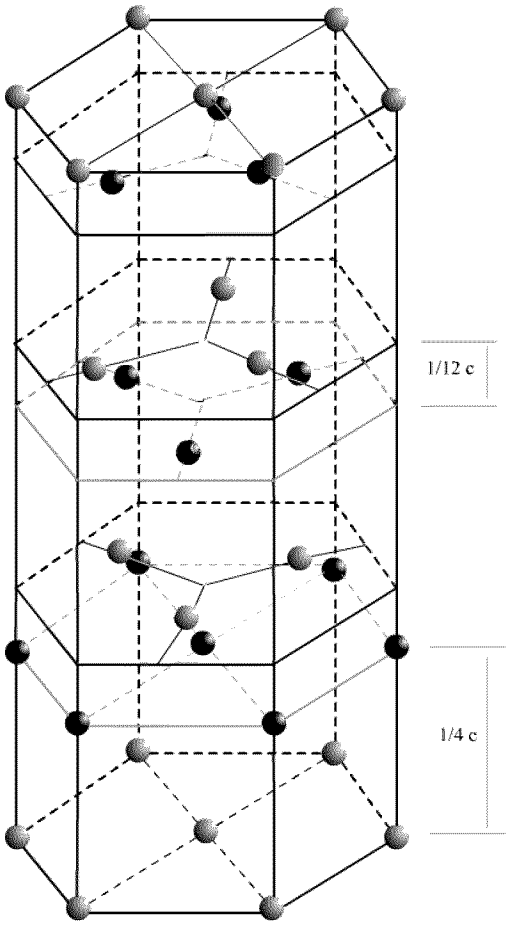

Fig. 1 Description of structure of diamond-like materials in hexagonal axises

Axis c is represented by body diagonal of cube [111] ($c = a\sqrt{3}$, a - parameter of cubic lattice). Atoms of one grade are located on highly densed planes {111}

A distance between two densely packed atomic layers A and A' is $d = c/4$ ($c = a^0\sqrt{3}$, a^0- parameter of cubic lattice). Atoms on these layers are in identical positions. And atoms in layers A' and B (B' and C) are displaced from each other on $\vec{\rho}_I = \frac{2}{3}\vec{a} + \frac{1}{3}\vec{b}$ for layers (A', B), or $\vec{\rho}_{II} = \frac{1}{3}\vec{a} + \frac{2}{3}\vec{b}$ - for (B' , C). Here $\vec{a}$ and $\vec{b}$ - vectors of hexagonal lattice on basic plane. A distance between these layers makes $c/12$.

A description of structure of diamond-like materials in hexagonal axes, excludes appearance of a problem associated with not identical deformation of materials on body diagonals [43].

Energy of interaction between atomic planes is calculated by means of interatomic potentials under a scheme presented previous work [46]. The aprioristic pseudo-potential [47] is used in calculations. In uniform model, from the first principles, deformations of diamond-like materials are presented at one axis compression and tension along direction [111].

The theory of pseudo-potential can be formulated in terms of pair potential, only in that case when ions are redistributed at constant average density of a material.

By the energy of interlayer interaction, a theoretical strength of diamond-like materials is calculated at one axis tension and compression in case of deformation [48]. At small deformations when one may neglect a change of average density of a material, a calculation of theoretical strength on the basis of interatomic potentials is justified.

In the present work we consider one axis deformation of materials when a volume per atom in a material remains constant. Changing one of parameters of hexagonal lattice, the second is defined from a condition of volume invariance. In this case the employment of pair interatomic potentials is justified for any possible deformation.

A complete energy of electron – ion system can be written as

$$U = U_0 + U_1, \qquad (1)$$

where U_0 - depends on volume, U_1 (energy of zone structure and a part of electrostatic energy) depends on structure and it can be performed as a sum

$$U_1 = \frac{1}{N}\sum_i \Phi(R_i) \qquad (2)$$

energies of pair interatomic potentials; R_i - interatomic distance. Energy of zone structure defines indirect effect between ions

$$U_{bs} = \sum\sum\sum \exp\left| i\vec{q}(\vec{R}_i - \vec{R}_j)\right| V^2(q)\chi(q)\varepsilon(q). \qquad (3)$$

Here $V(q)$ - pseudo potential of ions, $\vec{q}$ - wave vector and appearing functions $\varepsilon(q)$ and $\chi(q)$ are defined in [9]; $\vec{R}_i$ and $\vec{R}_j$ - radius vectors of ions.

Energy of zone structure (3) together with potential of direct interaction define a complete effective interaction among ions

$$\Phi(R)=\frac{Z^2}{R}+\frac{2\Omega_0}{(8\pi)^2}\int \exp(i\,\vec{q}\,\vec{R})\;U_{bs}(q)\,d\,\vec{q}\,, \qquad (4)$$

where Z - a number of valent electrons, Ω_0 - atom volume in elementary cell.

Let's sum (1.4) on two parallel highly densed layers distant from each other on d and shifted from each other on vector $\vec{\rho}$. For the energy of interaction of two layers (per square unit) we obtain [11]

$$\Phi(d,\rho)=\frac{1}{S}\sum\frac{2\Omega_0}{(2\pi)^2}\int\left[\Phi(q)+\frac{2\pi Z^2}{\Omega_0\,q^2}\right]\exp(i\,q_z d)\exp(i\,\vec{q}_\perp(\vec{R}+\vec{\rho}))\,d\,\vec{q}\,. \qquad (5)$$

Here S - area per atom in highly densed layer; vector $\vec{q}$ is divided on two components q_z - perpendicular highly densed plane and $\vec{q}_\perp$ - parallel to it. Through $\vec{R}_i$ - we designate lattice vectors lying in a plane of highly densed layer. To calculate integrals (5) we use equality

$$\sum\exp(i\,\vec{q}_\perp\,\vec{R}_i)=\frac{(2\pi)^2}{S}\sum_{g_\perp}\delta\,(\vec{q}_\perp-\vec{g}_\perp)\,. \qquad (6)$$

Through $\vec{g}_\perp$ - we designate vectors of two-dimensional lattice inverse to considered plane of highly densed lattice with constant a. Sum in the right part of equality (1.6) equals zero if only vector $\vec{q}_\perp$ does not coincide with one of the vectors of reciprocal lattice.

If we substitute (6) in (5) we obtain

$$\Phi(d,\rho)=\frac{d}{2\pi}\sum F(d,\vec{g}_\perp)\exp(i\,\vec{g}_\perp\vec{\rho})\,, \qquad (7)$$

where

$$F(d,\vec{g}_\perp)=\int(\Phi\left[(g_\perp^2+q_z^2)^{1/2}\right]+\frac{2\pi Z^2}{\Omega_0(g_\perp^2+q_z^2)})\exp(iq_z d)\,d\,q_z\,, \qquad (8)$$

and $q_z=\frac{2\pi}{d}m\,;\qquad m=0;\ \pm1;\pm2;\ \pm3.....,$

then

$$\Phi(d,\vec{\rho})=\frac{1}{S}\sum\sum F(d,\vec{g}_\perp)\cos(\vec{g}_\perp\vec{\rho})\,. \qquad (9)$$

To calculate $F(d,\vec{g}_\perp)$ we have to build the pseudo-potentials $V(q)$.

Pseudo potential of ions, accounting for materials structure in hexagonal axises one may represent as:

$$V(\vec{q})=\frac{1}{6}\left[V_A+V_B\,e^{-i\vec{q}\vec{\delta}_1}+V_A\,e^{-i\vec{q}\vec{\delta}_2}+V_B\,e^{-i\vec{q}\vec{\delta}_3}+V_A\,e^{-i\vec{q}\vec{\delta}_4}+V_B\,e^{-i\vec{q}\vec{\delta}_5}\right], \qquad (10)$$

where V_A, V_B - atomic pseudo potentials of components (for diamond $V_A=V_B$), $\vec{\delta}_i$ ($i=1,5$) radius vectors of atoms in elementary cell and $\vec{q}$ - radius vector of point of reciprocal space. For diamond-like materials $\vec{\delta}_i$ we obtain the following values:

$$\vec{\delta}_1=\frac{1}{4}\vec{c}\,;\ \vec{\delta}_2=\frac{2}{3}\vec{a}+\frac{1}{3}\vec{b}+\frac{1}{3}\vec{c}\,;\ \vec{\delta}_3=\frac{2}{3}\vec{a}+\frac{1}{3}\vec{b}+\frac{7}{12}\vec{c}\,; \tag{11}$$

$$\vec{\delta}_4=\frac{1}{3}\vec{a}+\frac{2}{3}\vec{b}+\frac{2}{3}\vec{c}\,;\ \vec{\delta}_5=\frac{1}{3}\vec{a}+\frac{2}{3}\vec{b}+\frac{11}{12}\vec{c}\,.$$

After substitution of (1.11) in (1.10), we obtain

$$V(q)=\frac{1}{6}\left[V_A+e^{-i\vec{q}\vec{c}\frac{1}{4}}V_B\right]\left[1+e^{-i\vec{q}(\frac{2}{3}\vec{a}+\frac{1}{3}\vec{b})}e^{-i\vec{q}\frac{1}{3}\vec{c}}+e^{-i\vec{q}(\frac{1}{3}\vec{a}+\frac{2}{3}\vec{b})}e^{-i\vec{q}\frac{2}{3}\vec{c}}\right], \tag{12}$$

and

$$V^2(q)=\frac{1}{9}\left[V_A+V_B\cos(q_z\frac{c}{4})\right]^2\times$$
$$\times\{3+2\left[\cos(q_z\frac{c}{3}+\vec{q}_\perp\vec{\rho}_I)+\cos(\frac{2}{3}q_z c+\vec{q}_\perp\vec{\rho}_{II})+\cos(\frac{c}{3}q_z+\vec{q}_\perp(\vec{\rho}_I-\vec{\rho}_{II})\right]\} \tag{13}$$

Table 1 presents calculated values of energy of interlayer interaction and lattice parameters (in atomic units) in equilibrium state of crystals and fig. 2 shows a dependence of stress vs. lattice parameter c as a material is deformed on axis c

Table 1 Energy of interlayer interaction Φ_0 and lattice parameters a_0 , c_0 at equilibrium state of crystal; stars mean a_0^* , c_0^* experimental values of lattice parameters

Crystal	$-\Phi_0\cdot 10^{-2}$	a_0	c_0	a_0^*	c_0^*
Diamond	0,25998	4,7969	12,007	4,76	11,86
BN	0,22528	4,8423	12,144	4,89	12,0
SiC	0,23109	5,735	14,372	5,817	14,23
AlN	0,13385	5,808	14,549	5,85	14,58

At known values of energy of interaction of layers strain tensor is defined from the ratio [45]

$$\sigma_z=\frac{1}{d}\frac{\partial\Phi(d,\vec{\rho})}{\partial e_z}, \tag{14}$$

where e_z - relative deformation, $\Phi(d,\rho)$ - energy of interaction of atomic layers of unit areas distant on d and shifted relatively each other on vector $\vec{\rho}$.

Energy of interaction of atomic layers as A, A' - ($\Phi(c/4,0)$) and A', B - ($\Phi(c/12,\rho)$) differ almost by an order. Theoretical strength is calculated on (1.9) at energy $\Phi(c/12,\rho)$ in five times higher than at energy $\Phi(c/4,0)$. Thus in brittle materials with cubic structure and subjected to one axis tension along direction [111], microcracks at first appear between atomic planes {111}, taking place on distance $c/4$. The material most likely fails on layers consisting from two atomic planes distant from each other on $c/12$.

Functional dependence of stress vs. interplane distance for diamond is illustrated on fig. 2.

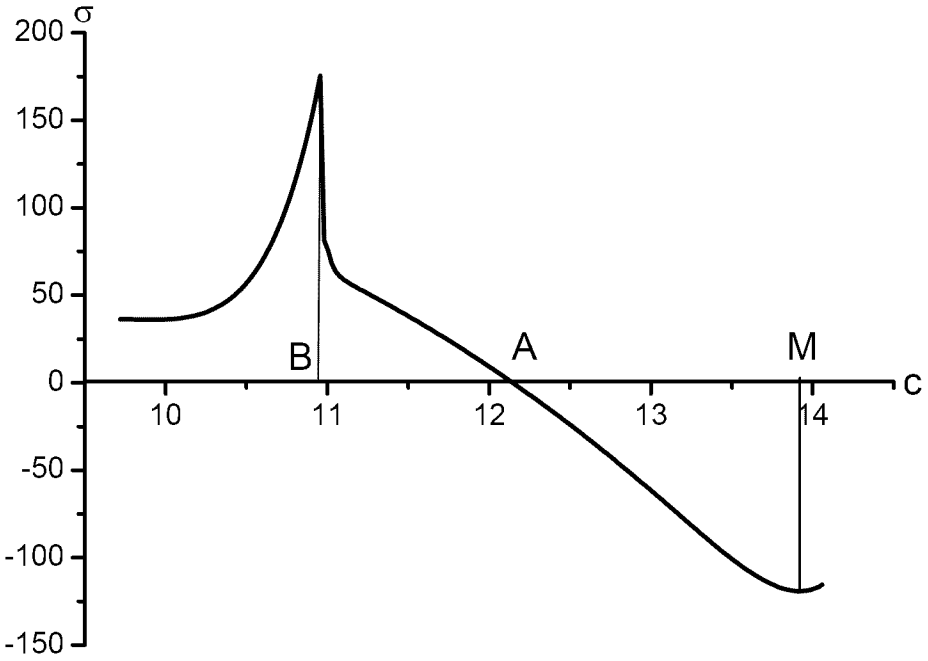

Fig.2 Dependence of stress σ vs. lattice parameter c for BN

A general view of this dependence is identical to the investigated materials. The interval BD corresponds to a cohesion zone ($\Phi(d,\rho)<0$). To the left of a point A a function describes compression process and to the right - tension. The point B corresponds to strength at compression, and D at tension.

At very small deformations a stress– strain curve is close to linear law, $\sigma = E\dfrac{\delta d}{d_0}$. From this ratio it is possible to define Young's modulus E.

Values of theoretical strength $\sigma_1^{\max}$, meeting deformation e_{111}^{*} at compression and $\sigma_2{}^{\max}$, e_{111}^{**} at tension as well as Young's modulus E are presented in tab. 2.

Table 2 Values of theoretical strength (GPa), Young's modulus (GPa) and strain rate at compression and tension

	Compression			**Tension**		
	$\sigma_1^{\max}$	$-e_{111}^{*}$	E_1	$\sigma_2{}^{\max}$	e_{111}^{**}	E_2
C	204,4	0,0975	1100	139,07	0,1456	1100
BN	175,4	0,0978	970	119,24	0,1458	970
SiC	147,56	0,0998	750	103,12	0,1459	750
AlN	88,26	0,098	450	59,05	0,1460	450

As it can be seen from the table, at one axis tension or compression a deformation corresponding to ultimate strength of diamond-like materials, possesses a certain value and does not depend on a material.

Surface energy of formed crack can be calculated proceeding from functional dependence of stress vs. interplane distance

$$\gamma = \int_{d_0}^{d_{\max}} \sigma(u)du . \qquad (15)$$

Here d_0 - distance between basic planes without deformation ($d_0 = {}^{c_0}\!/_{4}$), and $d_{\max}$ - corresponds to interplane distance when stress reaches its maximum value [12].

Finally for surface energy we obtain the following ratio

$$\gamma = \frac{\Delta\Phi}{e_{111}^{\bullet\bullet}} \cdot 7{,}78605 \cdot 10^{2} \quad \text{n/m} \qquad (16)$$

where $\Delta\Phi = \Phi(d_{\max}, \rho) - \Phi(d_0, \rho)$ - energy of deformation. The following values of energy of deformation are obtained at tension: $\Delta\Phi = 0{,}22195 \cdot 10^{-2}$ ($0{,}8081 \cdot 10^{-3}$) for diamond, $0{,}193595 \cdot 10^{-2}$ ($0{,}698 \cdot 10^{-3}$) - for boron nitride, $0{,}189 \cdot 10^{-2}$ ($0{,}855 \cdot 10^{-3}$) – for silica carbide and $0{,}113032 \cdot 10^{-2}$ ($0{,}44764 \cdot 10^{-3}$) – for aluminium nitride (in brackets we put the values of energy of deformation of compression). $Y_{1c} = 2\gamma$ is called as critical value of rate of release of deformation energy.

With calculation Y_{1c} thus there is a transition from values of microlevel to parameters of macrolevel. Calculation Y_{1c} at microlevel enables to define more precisely macrocharacteristics of materials, for example K_{1c} – fracture toughness coefficient at use of a ratio from macro-mechanics [51]

$$K_{1c} = \sqrt{Y_{1c} \cdot E}$$

Values Y_{1c}, K_{1c} at tension and compression are available in table 3.

Table 3 Macroscopic characteristics of diamond-like materials at tension (I) and compression (II)

	Y_{1c} n/m		K_{1c} MPa m$^{1/2}$		
	I	II	I	II	
Diamond	23,6728	12,839	5,1067	3,76075	$3{,}4-8$ [14]
BN	20,6484	11,0914	4,479	3,2832	$(3{,}5\pm0{,}5)$ [15]
SiC	20,1584	13,5858	3,89	3,194	-
AlN	12,056	7,113	2,33	1,79	-

Work [16] obtain the values K_{1c} for single crystal of cubic boron nitride in terms of (1-4) MPa*m$^{1/2}$ depending on the amount of impurities content. The calculated values Y_{1c} and K_{1c}, defined through deformations and energy of interaction of atomic layers, are found in terms of scattering of experimental values. Thus, the theoretical strength of diamond-like materials in determined crystallographic direction depends on a mutual positioning of cooperating layers. Densely packed atomic layers which are displaced relatively each other (on vector $\vec{\rho}_I$, or $\vec{\rho}_{II}$), are more stable at loadings, than not displaced layers. The strength in the first case is higher by an order than in the second one. Thus, at loadings along a direction [111] in diamond-like materials the cracks may appear, first of all, between densely packed atomic layers distant on ${}^{c}\!/_{4}$.

The calculated fracture toughness coefficient is in terms of accuracy of experimental values.

Critical deformation of diamond-like materials along direction [111] is a characteristic of structure and does not depend on a concrete material.

2. Investigation of influence of scale factor on theoretical strength of nanoparticle with diamond-like structure

A wide spectrum of practical applications of nanoparticles as base structural units of nanocomposites makes a theme of investigation of small particles actual. Since 80^{th} years the interest to small particles has brought to a lot of publications [55-60].

A direct experimental investigation of physico-mechanical properties of nanoparticles is rather complicated, as to obtain authentic results is not that simple methodical problem because of possible influence of scale factor on strength characteristics of tested samples [56]. Modeling of physico – chemical processes is complicated for these systems by a number of reasons. On the one hand, usual methods of quantum chemistry appear doubtful in application to a description of systems containing hundreds of atoms, and on the other hand, a macroscopic thermodynamics is inapplicable to small particles also because of impossibility of division of bulk and surface properties [57].

Among works of the last years a special place is occupied by publications which are devoted to definition of surface energy depending on particles form and size, with use of elements of macro- and micro - theories [57,58].

In work [58] to account for surface energy of nanoparticles, depending on their size and forms, the authors use a thermodynamic model. Surface energy is expressed through a surface tension at equilibrium condition of system. A consequence of given assumptions is, that all small particles are compressed by Laplacian pressure. Meanwhile, the experiment shows that not always lattice parameter for crystal particles decreases with a reduction of their sizes. The situations when lattice parameter does not vary even grows are rather often or. It means that at reduction of linear sizes of a particle surface forces are not always reduced to Laplacian pressure. At analysis of surface forces it is necessary to distinguish an equilibrium case when a body has the form corresponding to a minimum of system free energy and, nonequilibrium when it does not have this form. The body of nonequilibrium form under the action of Laplacian pressure aspires to obtain the equilibrium form [57]. In work [59] the authors define surface energy of nanoparticle through energy of break of bond between atoms. However, in this model the calculated surface energy depends only weak on type of structure of nanoparticles.

In works [61-62] authors assert that a basic arbitrariness in definition of nanoparticle size brings to ambiguity in definition of its many mechanical characteristics.

A problem of this investigation – is to build (being based on the method of aprioristic pseudo-potential) the analytical model which adequately would describe mechanical properties of nanoparticles in view of a role of advanced surface of particle.

For a description of a process of deformation of nanoparticles at one axis loading in this work we suggest to use a value of energy of interaction between atomic planes (perpendicular to axis of loading).

As nanoparticles according to [63], possess properties of a crystal; thus let's describe a structure of nano-diamond in hexagonal axes, chosen for the axis z a body diagonal of cube [111].

Energy of interaction between atomic planes is calculated by means of interatomic potentials which are built under above said scheme.

As models of nanoparticle let's use: a) nanoplate with final number of basic planes (l) on spatial axis z ; b) infinite nanobar with a basis of limited size on spatial axes x, y , and c) nanobar with limited nanosizes on three spatial axes.

Earlier it was shown that microcracks first of all appear between atomic planes {111}, distant on $c/4$, in massive brittle materials with cubic structure and subjected to one axis tension. The material most likely fails on layers consisting of two atomic planes distant from each other on $c/12$.

Fig. 3 schematically shows a nanoplate consisting of certain number of atomic planes (as pieces). Shaded strip correspond to strongly bonded atomic planes distant on $c/12$ (let's account for those as certain structural unit). Nanoplate is represented as a set of parallel structural units distant from each other on $c/4$.

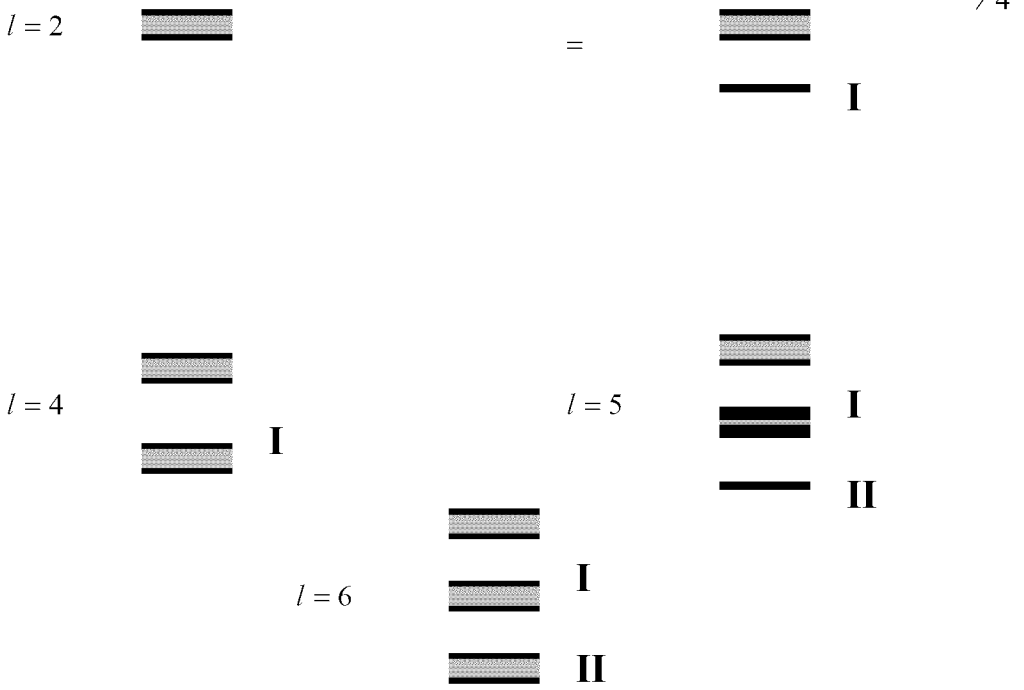

Fig. 3 Location of basic planes depending on their quantity l

At loading of nanoplate, a distance between neighboring layers changes. In ideal case (infinite material on three directions) the energy of interaction among those is Φ_0. For materials of limited size at calculation of energy of interaction among layers it is necessary to account for energy of external surfaces. In case of nanoplate we have two closing (atomic) surfaces. Generally the energy of interaction between neighboring structural units i. $i+1$ consists of two parts

$$\Phi_{i,i+1} = \Phi_0 + \sum_j \Phi^j_{i,i+1} \qquad (17)$$

Here $\sum_j \Phi_{i,i+1}^j$ - a share of energy of external surfaces.

Assuming, that external surface of nanoparticle possesses the energy which equals a half of energy of interlayer interaction (with the nearest absent atomic plane), it is possible to calculate the energy of interaction of atomic planes for chosen structural models.

If surface energy plays the main role at definition of mechanical characteristics of materials thus there appears a question about a presence of different values of theoretical strength of material depending on distance up to a surface. Closer to a surface a material has the higher strength than in volume. A solution of this problem is associated with calculation of energy of interaction between structural units depending on a distance of free surface.

Let's consider a semi-infinite sample which free surface coincides with highly densed plane. If for ideal case (infinite sample) the energy of interaction between neighboring structural units is Φ_0, because of a presence of energy of free surface of a particle, its value changes. Let's introduce a term "mesolayer", consisting of two parallel structural units, a distance between those makes $c/4$.

To define the energy of interaction between structural units at presence of free surface, we suggest use averaging on two neighboring mesolayers under the following scheme:

Let for 1st and 2nd mesolayer (fig. 3) the energy of interaction in zero order is Φ_0, and a free surface has energy $\frac{1}{2}\Phi_1$. Let's define the energy of interaction of 1st meso-layer as a simple average, from ratio

$$\Phi_I = \frac{1}{2}(\Phi_0 + \Phi_0 + \frac{\Phi_1}{2}) = \Phi_0 + \frac{\Phi_1}{2^2} \ . \qquad (18)$$

For 2nd meso-layer the energy of interaction we define falling from refined value of energy of 1st meso-layer

$$\Phi_{II} = \frac{1}{2}(\Phi_I + \Phi_0) = \Phi_0 + \frac{\Phi_1}{2^3}, \qquad (19)$$

and for j layer

$$\Phi_j = \Phi_0 + \frac{\Phi_1}{2^{j+1}} \ . \qquad (20)$$

Thus a distribution of surface energy on meso-layers is obtained depending on distance of external surface. If the object has limited size on spatial axis z then it is necessary to account for the influence of energy of 2nd surfaces. Let the second surface has the energy $\frac{\Phi_2}{2}$. The method of calculation of distribution of energy of interaction in view of 2nd external surface is the same, as above described. As a result we obtain for i layer

$$\Phi_i = \Phi_0 + \Phi_1 \frac{1}{2^{i+1}} + \Phi_2 \frac{1}{2^{j+2-i}} + \frac{1}{j \cdot 2^{j+1}}(\Phi_1 + \Phi_2), \qquad (21)$$

where j - a number of layers in nanoparticle. A number of layers j and a number of atomic layers l are connected with each other

$l = 2j$, then $\Phi_1 = \Phi_2$,

$l = 2j + 1$, respectively, $\Phi_1 \neq \Phi_2$; $\Phi_2 = \Phi_0$.

The last item in (2.5) provides the law of preservation of full energy of system at limited number of atomic planes l. The ratio (2.5) can be used for calculation of energy of interlayer interaction both for bulk samples and for nanoplates as well.

In case of infinite nanobar (the basic plane of nanoparticle has sizes na and mb (fig. 4), and the amount of those is infinite, n, m - integers), we account for energy of lateral surfaces.

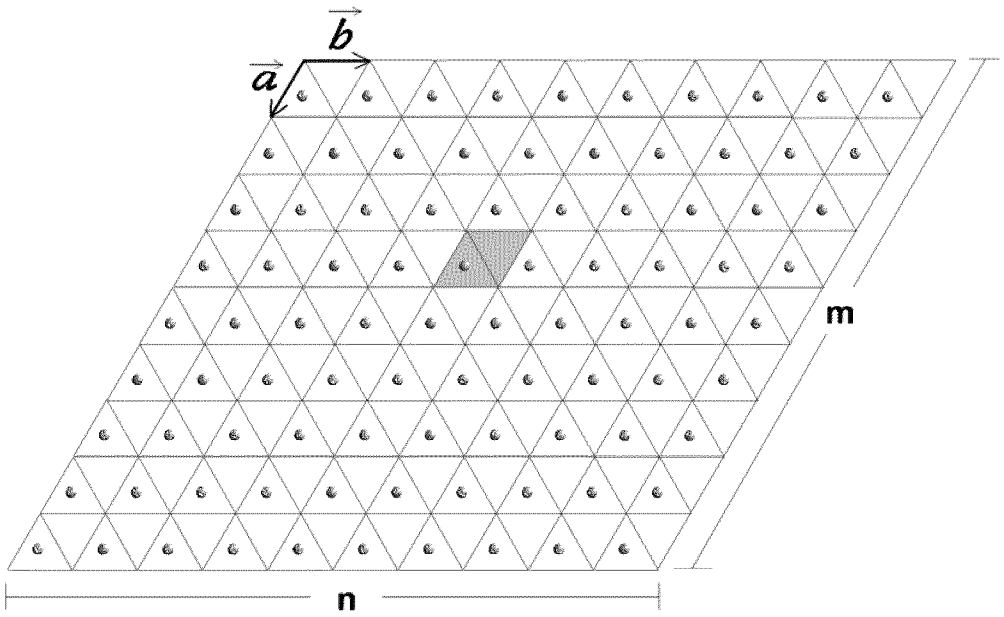

Fig.4. Basic plane of diamond-like materials in hexagonal axises a, b, axis c is perpendicular to the plane

According to problem condition, we calculate mechanical characteristics at one axis loadings, using the energy of interaction between structural units. The last are perpendicular to the axis of loading. Therefore, in lieu of lateral surfaces we consider lateral atomic lines on planes. The energy of interaction between lateral atoms, located on neighboring planes, represents a required share of surface energy. Thus, the energy of interaction between atomic layers (2.1) can be presented as

$$\Phi = (N_1 \Phi_0 + N_2 \Phi_B)/(N_1 + N_2), \tag{22}$$

where N_1 – a number of atoms on planes located inside a nanobar, N_2 - extreme atoms of these planes, Φ_B - energy of interaction between extreme atoms in neighboring layers. In this case

$$N_1 = (n-2)(m-2) \text{ and } N_2 = 2(m+n-2) \tag{23}$$

Accounting for a number of bonds of extreme and angle atoms of nano-diamond on basic planes for energy of meso-layer interaction we obtain

$$\Phi = \Phi_0 \left[1 + \frac{1}{3}\left(\frac{1}{m} + \frac{1}{n}\right) - \frac{8}{9mn} \right], \tag{24}$$

when a basic plane is a parallelogram with sides ma and nb, and

$$\Phi = \Phi_0 \left[1 + \frac{1}{3}\left(\frac{1}{m} + \frac{1}{n}\right) + \frac{5}{3mn} \right], \qquad (25)$$

for a rectangle with sides ma $\frac{\sqrt{3}}{2}$ and nb and with equal basic square.

If m, $n \to \infty$, then $\Phi \to \Phi_0$.

In case of limited bar or nanobar for i layer we obtain

$$\Phi_i = \Phi_0^* + \Phi_1^* \frac{1}{2^{i+1}} + \Phi_2^* \frac{1}{2^{j+2-i}} + \frac{1}{j \cdot 2^{j+1}} \left(\Phi_1^* + \Phi_2^* \right) \quad . \qquad (26)$$

.

Here $\Phi_k^* = \Phi_k \left[1 + \frac{1}{3}\left(\frac{1}{m} + \frac{1}{n}\right) - \frac{8}{9mn} \right]$, (27)

or

$$\Phi = \Phi_0 \left[1 + \frac{1}{3}\left(\frac{1}{m} + \frac{1}{n}\right) + \frac{5}{3mn} \right], \qquad (k = 0,\ 1,\ 2) \qquad (28)$$

At known values of energy of meso-layer interaction, a strain tensor is defined from the ratio

$$\sigma_z = \frac{1}{d} \frac{\partial \Phi(d)}{\partial e_z}, \qquad (29)$$

where e_z - relative strain rate, $\Phi(d)$ - energy of interaction of atomic layers in elementary cell distant on d.

Dependence of theoretical strength on distance up to external surface of nano-diamond (i -a number pf meso-layer) from size of a basic plane (m, n), from nanobar height, or nanoplate thickness (l, at fixed number of meso-layer) is illustrated in fig. 5-7.

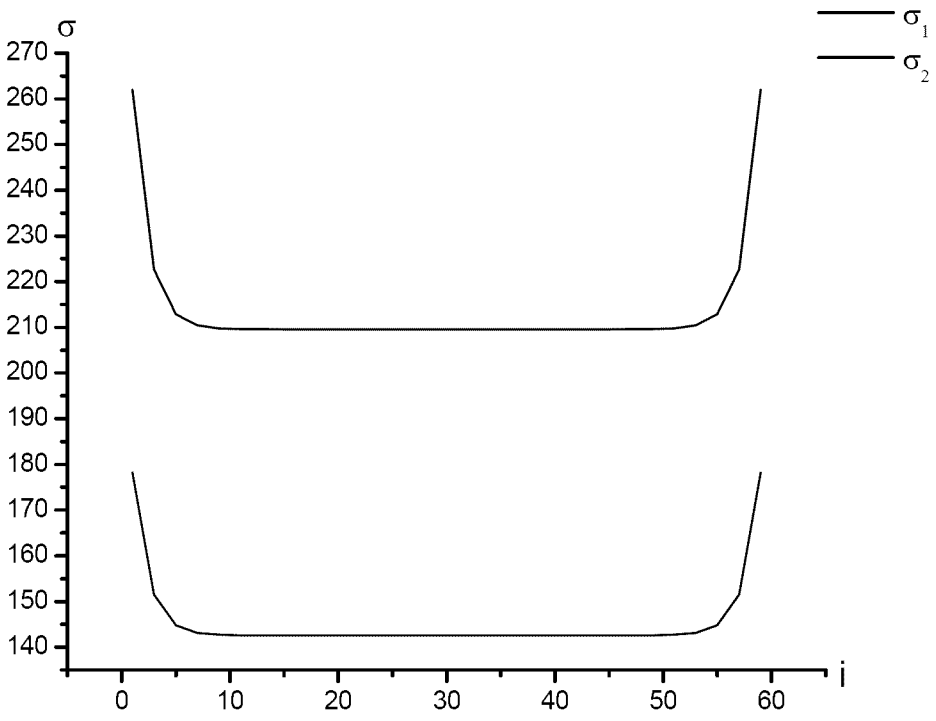

Fig.5 Dependence of theoretical strength of diamond nanoparticle vs. distance from external surface (vs. a number of mesolayer i, $l = 120$; $m = n = 25$)

Fig. 6 Dependence of theoretical strength of diamond nanoparticle vs. size of basic area (vs. m, n), when $l = 120$, a $i = 3$

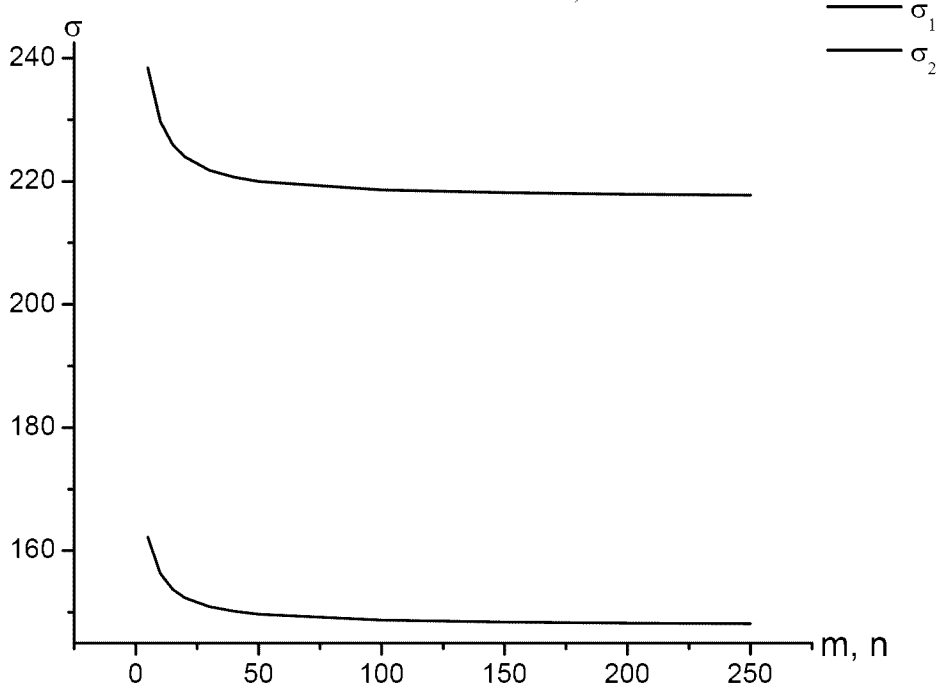

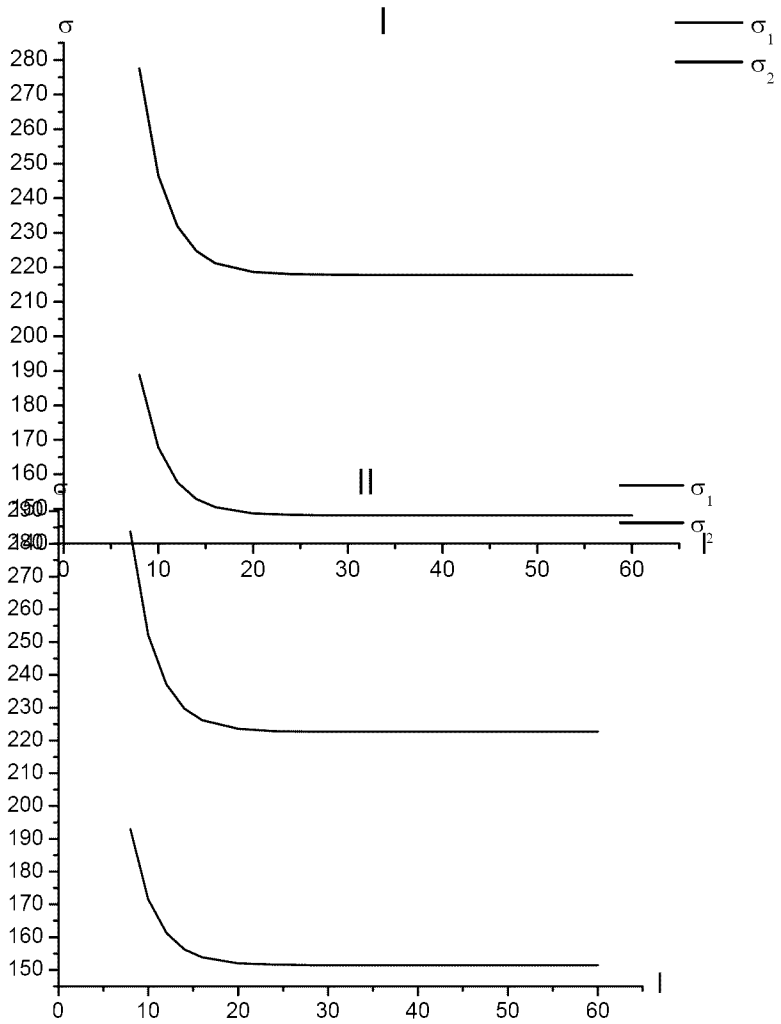

Fig. 7 Dependence of theoretical strength of nano-diamond vs. length (or l - a number of atomic layers) nanobar, when I - $m = n = 250$, and II - $m = n = 25$. In both cases $i = 3$

In a case of nanobar, consisting from 120 highly dense packed atomic planes, on distance from a surface $h_1 = a^* \sqrt{3} \frac{50}{6}$ (a^*-parameter of cubic lattice), value of theoretical strength at compression and tension is minimum (see fig. 3). At even values l a theoretical strength varies depending on distance up to external surface as symmetric function that can not be said about nanoparticle, containing odd number of densely packed atomic layers (see fig. 1). At odd number of atomic layers external surfaces of nanoparticles possess different energy that results in asymmetrical distribution of energy on nanobar length. At increase of a number of atomic planes a common picture of distribution of energy does not vary. In case $l = 1200$, on distance from the first surface $h_1 = a^* \sqrt{3} \frac{50}{6}$ and from the second surface $h_2 = a^* \sqrt{3} \frac{l}{6} - h_1$, a value of theoretical strength does not vary and coincides with a value of theoretical strength for massive samples (tab. 4).

Table 4 presents values of theoretical strength at compression σ_1 and tension σ_2 for diamond-like nanoparticles as nanobar, depending on its size and form of basis (rectangular or parallelogram).

Table 4 Value of theoretical strength (GPa) for diamond-like nanoparticles depending on their size and form of its basis (basic plane). Here l - a number of atomic layers, m, n - integers responsible for size of nanobar basis and i - a number of meso-layer describing a distance to external surfaces

	Nanobar with rectangle basis		Nanobar or nanoplate with parallelogram basis			
	$l = 100;\ m = n = 25$ $i = 2$		$l = 100; m = n;$ $i = 2$		$l = 120;\ m = n = 2500$ $30 \le i \le 570$	
	σ_1	σ_2	σ_1	σ_2	σ_1	σ_2
C	236,709	161,048	235,768	160,4	204,4	139,07
BN	203,14	138,087	202,3	137,5	175,4	119,24
SiC	170,88	119,42	170,203	118,94	147,56	103,12
AlN	102,208	63,385	101,802	68,113	88,26	59,05

Let's note, that at values $m = n = 2500$, theoretical strength at compression and tension for nanoplate with the basis of rectangular or parallelogram, do not differ from each other. Investigation (computing experiment) showed that at values $m = n \ge 500$ a value of theoretical strength (at tension and compression) does not depend on the form of basic area. Comparative calculations by an example of SiC nanobar with the basis of rectangular and parallelogram is presented in tab. 5.

Table 5 Dependence of theoretical strength of SiC nanobar vs. the form of basic area (I- parallelogram, II – rectangle)

Form		$m = n$ $= 25$	$m = n$ $= 50$	$m = n$ $= 100$	$m = n$ $= 150$	$m = n$ $= 200$	$m = n$ $= 300$	$m = n$ $= 500$
I	σ_1	180,023	179,845	178,709	178,323	178,129	177,934	177,777
I	σ_2	127,207	125,68	124,89	124,62	124,486	124,349	124,24

II	σ_1	182,749	180,027	178,75	178,34	178,14	177,939	177,777
II	σ_2	127,715	125,80	124,92	124,63	124,49	124,353	124,24

3. CONCLUSION

- Strength of nanoparticles at one-axis deformations strongly depends on particle size along the axis of loading and distances from external surface of particle;

- Theoretical strength of nanobar (nanoplate), at even value of atomic planes, along the axis of deformation on identical distances from external surfaces, has identical values. It is associated with identical energy of free surfaces of nanoparticle, unlike nanoparticles with odd number of planes. For nanoplate with size $h \geq a^* \sqrt{3} \frac{50}{3}$, a value of theoretical strength on distance $\frac{h}{2}$ from external surface always aspires to a value for massive samples.

- Theoretical strength does not depend on the form of nanobar basis of at values of basis area $S \geq 44200\, a^{*2}$.

IV. **Ballistic limit velocity. Theory and Experimental Approximation on the Base of Indentation Technique (A4 New Empirical Law for Critical Velocity of Penetration)**

TABLE OF SYMBOLS

ρ_p – density of KEP material;

ρ_t – density of target material;

L_p – projectile length;

u – velocity of movement of a contact surface;

R – static penetration resistance of target material (defined by analytical solution of a problem of expansion of spherical cavity);

t – time, s;

u_S – impact velocity;

V_{cr} – ballistic limit velocity;

h_t – target thickness;

Y – yield stress of target material;

HV – Vickers hardness of target material;

HM – Meyer hardness of materials;

δ_H – plasticity characteristic of target;

d_p – projectile diameter;

m_p – projectile mass;

bottom indexes t and p respectively are referred to target and projectile.

INTRODUCTION

In a problem of interaction of kinetic energy projectile (KEP) with a target a calculation of ballistic limit velocity V_{cr} represents a significant scientific and theoretical interest. A process of penetration of indenter into target has much in common with a process of indentation of a material with rigid indenter. In this work, being based on the representations about indentation process elaborated by authors the problem of calculation of ballistic limit velocity is submitted on the basis of experimental results obtained at indentation (microhardness HV and plasticity characteristic δ_H). The theory of calculation V_{cr} for a case of not deformable projectile is offered as well. For the common case (deformable and not deformable projectile) empirical equations which enable to calculate V_{cr} with satisfactory accuracy are suggested

1. Dynamic tests of materials

In this work we investigated a wide class of target materials: aluminum alloys (standard and high-strength, developed in IPMS NAS of Ukraine), titanium alloy, steels (soft and strengthened) and ceramics. A choice of objects of investigations is stipulated by a necessity to obtain the materials with a wide range of physico-mechanical properties. It, in its turn, was necessary to obtain rather representative experimental data file on the basis of which it would be possible with a rather good reliability to define regularities for ballistic limit velocity of penetration. Thickness of targets, geometrical sizes and a material of projectile were varied as well.

A chemical composition of the investigated alloys is presented in table 1, and physicomechanical properties - in table 2.

Samples for tests represented the plates of 100x100 mm of various thicknesses, which were fixed in holder's slot. The holder was steel thermo-treated plate (HRC 40) with thickness of 40 mm. The plate has square reach-through hole of 50x50 mm for free flight of kinetic projectile in case of penetration of tested sample. The holder, in its turn, was rigidly installed in the frame of machine (Fig.1). With the help of this holder the sample can be located in required position i.e. to provide a hit of projectile in certain place of the sample (with an accuracy ± 5mm) and under a certain angle to sample plane (in this work this angle was 90^0).

Fig 1 Equipment for dynamic tests

A distance from a channel cut of missile machine to a sample plane made 10 m. Projectile velocity was fixed by means of serially produced device "Polet" with an accuracy of 0.1 m/s. A principle of velocity registration – fixing of time of projectile flight between two photo sensors established on a distance of 0.5 m.

With the purpose to increase a reliability of test results a thick polyethylene film was mounted behind a tested plate on distance of 30 mm. The plane of film tension was in parallel to a plane of plate. The fact of plate penetration was considered as defined at presence of reach-through hole in the film.

2. Theoretical estimation of ballistic limit velocity

Calculation of ballistic limit velocity of a material for a case of not deformable projectile (when its hardness considerably exceeds the hardness of target) is suggested. A theoretical substantiation is given below.

The equation of projectile movement in infinite target is considered and it looks as:

$$\rho_p L_p \frac{du}{dt} = -\frac{1}{2}\rho_t u^2 - R, \quad u(0) = u_s . \tag{1}$$

This equation, in essence, is a special case of the equation of V.P. Alekseevskii [1] if in the last to assume that projectile is not deformable.

Equation (1) is an equation with divided variables and its solution can be presented as

$$\frac{\rho_t}{2L_p\rho_p}t = \frac{1}{a}\left(arctg\frac{u_S}{a} - arctg\frac{u}{a}\right), \qquad a^2 = \frac{2R}{\rho_t},$$

or

$$u(t) = a\frac{u_S - a\cdot tg\left(\dfrac{a\rho_t t}{2L_p\rho_p}\right)}{a - u_S tg\left(\dfrac{a\rho_t t}{2L_p\rho_p}\right)}, \qquad a = \sqrt{\frac{2R}{\rho_t}}. \tag{2}$$

For penetration depth P from equation (1) we obtain

$$P = \int_0^t u(\tau)d\tau = -\int_{u_s}^{u} u\frac{2\rho_p L_p}{\rho_t}\frac{du}{a^2+u^2} = \frac{\rho_p L_p}{\rho_t} ln\frac{a^2+u_S^2}{a^2+u^2} \tag{3}$$

If from (2), (3) to exclude u, then we obtain a dependence of penetration depth vs. time t

$$P(t) = \frac{\rho_p L_p}{\rho_t} ln\left[\frac{\left(a^2+u_S^2\right)(a-tg\gamma)^2}{a^2\left((a-tg\gamma)^2+(u_S-tg\gamma)^2\right)}\right], \qquad \gamma = \frac{a\rho_t t}{2L_p\rho_p}$$

Ballistic limit velocity V_{cr} is approximately determined from (3) as impact velocity $u_S\left(=V_{cr}\right)$, at which $P = h_t$ and $u = 0$ (i.e. projectile stops), where h_t - target thickness. Therefore from (3) we obtain

$$h_t = \frac{\rho_p L_p}{\rho_t} ln\left(1+\frac{V_{cr}^2}{a^2}\right). \tag{4}$$

from this equation for velocity V_{cr} we have

$$V_{cr} = a\sqrt{exp\left(\frac{\rho_t h_t}{\rho_p L_p}\right)-1} = \sqrt{\frac{2R}{\rho_t}\left[exp\left(\frac{\rho_t h_t}{\rho_p L_p}\right)-1\right]}. \tag{5}$$

Introducing a designation $\alpha = \frac{\rho_t h_t}{\rho_p L_p}$ let's re-write formula (5) as:

$$V_{cr}^2 = \frac{2R}{\rho_t} \cdot \left(e^{\alpha} - 1\right) \qquad (5')$$

For ideal elastic-plastic material for R one may use formula [22]

$$R = Y\left(\frac{2}{3} + ln\frac{2E}{3Y}\right). \qquad (6)$$

At the same time R may be estimated as the function of HV. In work [3] it was shown, that at estimation of target resistance against penetration of a kinetic energy projectile it is necessary to account for plasticity characteristic δ_H determined (as hardness HV), at indentation of a material by Vickers's indenter [4]. A product of resistance of target material R on plasticity characteristic δ_H (or product $HM \cdot \delta_H$) enables to allocate a part of resistance associated with plastic deformation of a material at penetration of kinetic energy projectile.

In a view of the above said, 3 variants of estimation R are carried out with the aim of achievement of best agreement of theory and experiments (table 2).

Table 1 Chemical composition of target material

Material groups	Material marking	Chemical composition, mass.%	*HV*, GPa	δ_H
Al-alloy	6112	Al – 1Mg – 0.3Cu – 0.6Si	0.84	0.92
	АМГ-5	Al –5Mg	0.80	0.93
	8112	Al – 8Zn – 2.1Mg – 1.9Cu – 0.15Zr	1.80	0.84
	8312	Al – 8Zn – 2.1Mg – 1.9Cu – 0.15Zr – 0.12 Sc	1.9	0.82
Steel	Steel 124	Fe – 0.38C – 0.25Si – 0.035Cr – 1.6Mn – 0.013 Ni – 0.41Mo	3.7	0.85
	Steel 600	Fe – 0.68C – 0.29Si – 0.61Cr – 0.77Mn – 1.87 Ni – 0.32Mo	6.72	0.71
	Steel 40	Fe – 0.38C – 0.36Si – 0.08Cr – 0.9Mn – 0.12 Ni – 0.12Mo - 0.07Cu	2.02	0.922
	High hardness steel	Fe – 0.25C – 0.36Si – 0.27Cr – 0.9Mn – 1.0Ni – 0.3Mo – 0.19Cu	3.45	0.866
Ti-alloy	Ti-alloy	Ti – 5.1V – 0.3Fe – 0.4Si – 3.0Al	3.22	0.854
Ceramics	SiC	Self-bounded silica carbide	22	0.35
Metallic plates (dams), used for experiments with ceramics	П1	Steel 45 raw (TP free)	1.81	0.93
	П2	Steel 45 (hardening + tempering)	3.22	0.88
	П3	AMG 5	0.80	0.93
	П4	High hardness steel Fe – 0.25C – 0.36Si – 0.27Cr – 0.9Mn – 1.0Ni – 0.3Mo – 0.19Cu	3.45	0.866

Table 2 Results of dynamic tests of materials for the case of «not deformable projectile»

Material class	Material	Target thickness h_t, mm	d_p, mm	L_p, Mm	ρ_t, g/sm^3	HV_t GPa	δ_{Ht}	HV_p GPa	δ_{Hp}	$\sigma_{0.2}$, GPa	$R(3)$ GPa	V_{cr}^{actual} m/s	Calculation by formula (5)		
													$V_{cr}^{calcul}(1)$ m/s	$V_{cr}^{calcul}(2)$ m/s	$V_{cr}^{calcul}(3)$ m/s
Al-alloys	6112	8	7.62	26	2.7	0.84	0.92	1.6	0.93	0.26	1.406	**323**	251	326	340
	AMG 5	5	9	12	2.7	0.80	0.93	1.6	0.93	0.25	1.372	**387**	290	379	393
	8112	8	7.62	20.5*	2.8	1.8	0.84	1.9	0.93	0.56	2.503	**438**	418	522	569
	8312	8	7.62	20.5*	2.8	1.9	0.82	1.9	0.93	0.59	2.561	**456**	425	524	579
	AMG5	5	7.62	16	2.7	0.80	0.93	1.78	0.93	0.25	1.372	**290**	249	325	337
Steels	Steel 40	40.5	12.7	51.6*	7.8	2.02	0.922	6.55	0.746	0.4	2.388	**845**	784	854	889
	High hardness steel	16.5	12.7	51.6*	7.8	3.45	0.866	6.55	0.746	0.95	4.660	**685**	558	671	721
	Steel 45	3	7.62	12.5*	7.8	1.81	0.93	1.6	0.93	0.5	2.409	**470**	355	409	424
Ti-alloy	Ti-alloy	17	12.7	51.6*	4.6	3.22	0.854	6.55	0.746	1.0	2.849	**490**	526	515	557

*- for given materials in calculations we used core length but not projectile as jacket fails at penetration

$$R(1) = HM \cdot \delta_H$$

$$R(2) = Y\left[\frac{2}{3} + ln\left(\frac{2E}{3Y}\right)\right] \cdot \delta_H \quad (Y = \sigma_{0,2})$$

$$R(3) = Y\left[\frac{2}{3} + ln\left(\frac{2E}{3Y}\right)\right]$$

$$\alpha = \frac{\rho_T h_t}{\rho_p L_p}$$

The best coincidence of theory and experiment gives the variant (2) in which the parameter δ_H is accounted for. In this case experimental and theoretical results (obtained without fitting parameters) almost coincide.

As it's already been said above, the suggested theoretical estimation is applicable only for a case when projectile hardness considerably exceeds hardness of target. It is well seen at the analysis of results for alloys 8112 and 8312 where projectile and target hardness are close. Divergences of theory and experiment here are more essential.

3. Empirical estimation of ballistic limit velocity

For more common case of an estimation of ballistic limit velocity (including a deformable projectile) semi-empirical formulas are suggested.

On the basis of available in literature and obtained by authors results the following empirical equations for parameter V_{cr} are suggested:

$$V_{cr}^2 = C_1 \rho_t \frac{h_t}{P} \tag{7}$$

$$V_{cr}^2 = C_2 \rho_t \frac{h_t}{P} (HV\delta_H)_t \tag{8}$$

$$V_{cr}^2 = C_3 \rho_t \frac{h_t}{P} \frac{(HV\delta_H)_t}{(HV\delta_H)_p} \tag{9}$$

C_1, C_2, C_3 are the empirical constants determined by available experimental results (in our case – according to tests of 10 different materials) by determination of average arithmetic value. P is so-called static pressure of projectile on target.

$$P = \frac{m_p}{\pi d_p^2 / 4},$$

where m_p and d_p – projectile's mass and diameter respectively.

Experimental results and calculations under formulas (7), (8) and (9) are presented in table 3.

Formula (7) is most simple and demands a minimum of initial data for calculation V_{cr} which are easy to obtain by direct measurement and weighing. However, a coincidence of calculated and experimental data is not enough. The error reaches 40 % and higher (for steel 600 in particular). Though for ceramics and high-strength aluminum alloys (8112 and 8312) a quite good conformity is observed.

Formula (8) provides as a whole the higher accuracy (especially for aluminum alloys) though the values of micromechanical properties of target (hardness and plasticity characteristic) are necessary for calculation. For ceramics this formula does not work (an error up to 80%).

And at last there comes formula (9). For calculation, besides micromechanical properties of target, knowledge of projectile properties is required. Calculation under this formula gives the best agreement of

calculated and actual values V_{cr}. The error of calculation does not exceed 5-6% for metals and 8-10 % for ceramics and only in some cases reaches 15-20% for ceramics SiC (the explanation of this is given below).

The analysis of the above-stated empirical dependences enables to draw the following conclusion. For the most correct calculation V_{cr} it is necessary to account for mechanical properties of both target and projectile (besides their geometrical sizes as well as their density and mass). Therefore further it is expedient to use formula (9) for calculations, as it provides the greatest accuracy.

It is should be noted that at calculation V_{cr} for composite targets "ceramics - dam" a ratio was used:

$$V_{comp}^2 = V_{cer}^2 + V_{back}^2 ,$$

where V_{cer} and V_{back} are the ballistic limit velocities of penetration of ceramic target and dam respectively.

Table 3 Dynamic test results

Materials Class	**Alloy**	ρ_t g/cm^3	h_t mm	m_p g	d_p mm	L_p mm	HV_t GPa	δ_{Ht}	HV_p GPa	δ_{Hp}	V_{cr}^{actual} **m/s**	$V_{cr}^{calcul}(1)$ empirical m/s	$V_{cr}^{calcul}(2)$ empirical m/s	$V_{cr}^{calcul}(3)$ empirical m/s
Al-alloys	6112	2.7	8	7.9	7.62	26	0.84	0.92	1.6	0.93	**323**	435	276	330
	АМГ 5	2.7	5	5.9	9	12	0.8	0.93	1.6	0.93	**387**	474	295	353
	8112	2.8	8	3.6*	7.62	20.5*	1.8	0.84	1.9	0.927	**438**	457	405	447
	8312	2.8	8	3.6*	7.62	20.5*	1.9	0.82	1.9	0.927	**456**	457	411	453
	АМГ5	2.7	5	5.5	7.62	16	0.8	0.93	1.80	0.93	**290**	412	256	289
Steels	Steel124	7.8	4.5	4.8*	7.62	26*	3.7	0.85	1.78	0.931	**689**	508	649	737
	Steel600	7.8	4.5	4.8*	7.62	26*	6.72	0.71	1.78	0.931	**916**	508	799	906
	Steel40	7.8	40.5	30.1*	12.7	51.6*	2.02	0.922	6.55	0.746	**845**	1219	1200	794
	High hardness steel	7.8	16.5	30.1*	12.7	51.6*	3.45	0.866	6.55	0.746	**685**	779	970	642
	П 1	7.8	3	4.8*	7.62	26*	1.81	0.93	6.55	0.746	**<280**	412	385	255
	П 1	7.8	3	2.3*	7.62	12.5*	1.81	0.93	1.80	0.93	**470**	542	507	574
	П 2	7.8	3	2.3*	7.62	12.5*	3.22	0.88	6.55	0.746	**328**	412	500	331
	П 4	7.8	4.5	3.6*	7.62	20.5*	3.45	0.866	6.55	0.746	-	582	726	480
	П 4	7.8	4.5	30.1*	12.7	51.6*	3.45	0.866	6.55	0.746	-	406	507	335
Ti-alloy	Ti-alloy	4.6	17	30.1*	12.7	51.6*	3.22	0.854	6.55	0.746	**490**	606	725	480
Ceramics	SiC	3.09	8	4.8*	7.62	26*	22	0.35	6.55	0.746	-	423	846	560
	SiC	3.09	6	3.6*	7.62	20.5*	22	0.35	6.55	0.746	-	423	846	560
	SiC	3.09	10	30.1*	12.7	51.6*	22	0.35	6.55	0.746	-	381	763	505
	SiC	3.09	12	30.1*	12.7	51.6*	22	0.35	6.55	0.746	-	418	836	553
	SiC	3.09	15	30.1*	12.7	51.6*	22	0.35	6.55	0.746	-	467	934	618
	SiC + П 1		8+3	4.8*	7.62	26*			6.55	0.746	**660**	590	930	615
	SiC + П 2		8+3	4.8*	7.62	26*			6.55	0.746	**710**	590	983	650
	SiC + П 3		8+5	4.8*	7.62	26*			6.55	0.746	**660**	526	869	606
	SiC+П4		6+4.5	3.6*	7.62	20.5*			6.55	0.746	**730**	719	1115	738

* – for given materials in calculations we used length and mass of core but not projectile, as jacket fails at penetration;

Projectile's density ρ_p in all cases was accepted as 7.8 g/cm^3.

Values of empirical constants C_1, C_2 and C_3 were 1.52×10^6 m^2/s^2, 0.79×10^6 m/kg and 1.69×10^6 m^2/s^2 respectively.

This equation we obtained from the law of conservation of energy. It was supposed, that kinetic energy of projectile was consistently spent on penetration through ceramic target and dam. Projectile's mass in a process of penetration was considered as constant. It, probably, not absolutely meets a reality. Projectile while going through ceramics loses a part of mass and only the rest part of projectile influences on a dam. Therefore a real value V_{back} (and V_{comp}) must be higher than calculated one). It takes place.

Let's get back to formulas (7) – (9). Approximately while considering a projectile as a cylinder, let's find its volume $V = \frac{\pi d_p^2}{4} L_p$, where L_p is the projectile's length. Density of projectile's materials is:

$$\rho_p = \frac{m_p}{V} = \frac{m_p}{\frac{\pi d_p^2}{4} L_p}$$

Since $\frac{m_p}{\pi d_p^2 / 4} = P$, then $\rho_p = P / L_p$ or $P = \rho_p L_p$. By introduction of designation α, used in theoretical formula (5'):

$$\alpha = \frac{\rho_t h_t}{\rho_p L_p},$$

formulas (7) – (9) one may write as:

$$V_{cr}^2 = C_1 \alpha \qquad (7')$$

$$V_{cr}^2 = C_2 \alpha (HV\delta_H)_t \qquad (8')$$

$$V_{cr}^2 = C_3 \alpha \frac{(HV\delta_H)_t}{(HV\delta_H)_p} \qquad (9')$$

The empirical dependences written down in this form obtain some physical sense. Let's decipher formula (9 '), as the most correct.

Let's note, that parameters α in formulas (7') - (9') and (5) are completely similar. And accounting for that at $\alpha << 1$ (that takes place in our case) $exp\,\alpha - 1 \cong \alpha$ a certain similarity between the above said formulas is observed. A difference of formula (9') is that it accounts for projectile properties that are required for our case when a projectile can be deformed.

Also it should be noted that the authors of this project had introduced a concept of material resistance to penetration, determined as $HV \cdot \delta_H$ [64]. Thus $(HV \cdot \delta_H)_t$ is the resistance against penetration of target material (which is used here in lieu of that one calculated by formula (6)). By analogy let's introduce a concept $(HV \cdot \delta_H)_p$ as the penetrating ability of projectile material.

In view of it, it is possible to say that a square of ballistic limit velocity is directly proportional to specific surface mass of target and resistance to penetration of target material and inversely to specific surface mass and penetrating ability of projectile material (formula (9')).

The constant in equation (9') is numerically equal to a square of ballistic limit velocity of penetration of a target by projectile made from the same material and with a length equal to target thickness.

4. Comparative characteristic of dynamic resistance of different materials

Being based on the obtained experimental results and formula (9) the estimation of dynamic resistance of investigated materials is carried out. As a criterion a critical value $(\rho_t h_t)_{cr}$ of target material (representing its specific surface mass) at which the material withstands an influence of projectile of certain type moving with a speed V_p is accepted. Along with it a critical thickness of target material $h_{t\,cr}$ is defined. Results of calculations are presented in table 4.

The obtained data witness that the least dynamic resistance is attributed to soft aluminum alloys. Further come high-strength aluminum alloys and soft steel 40. Then (in terms of increase of dynamic resistance) we have titanium alloy and high-strength steel. Then – super high-strength steel 600. And at last ceramics SiC which possesses the best dynamic resistance from the investigated materials. It should be noted, however, that in practice the advantage of ceramics is not that impressive. The reason is that ceramics requires so-called "dam" (usually – a steel plate), providing for a required rigidity for tested sample and interfering its fracture immediately from a dynamic impact. A presence of dam brings a parameter $\rho_t h_{t\,cr}$ to increase for a composite target "ceramic + dam" (see table 4).

Table 4 Dynamic resistance of materials against penetration of different projectiles

Target material	Projectile material	HV_t GPa	δ_{Ht}	ρ_p g/sm^3	L_p mm	$(HV \cdot \delta_H)_p$	ρ_t g/sm^3	V_p =700 m/s		V_p =1000 m/s		V_p =1500 m/s	
								$(\rho h)_{t\,cr}$ g/sm^2	$h_{t\,cr}$ mm	$(\rho h)_{t\,cr}$ g/sm^2	$h_{t\,cr}$ mm	$(\rho h)_{t\,cr}$ g/sm^2	$h_{t\,cr}$, mm
6112	**Soft steel, (HV_p = 1.9GPa, δ_{Hp}=0.93**	0.84	0.92	7.8	26	1.67	2.7	12.7	47.2	26.0	96.3	58.5	216.6
AMG5		0.8	0.93	7.8	26	1.67	2.7	13.2	49.0	27.0	100.0	60.8	225.0
8112		1.8	0.84	7.8	26	1.67	2.8	6.5	23.3	13.3	47.4	29.9	106.8
8312		1.9	0.82	7.8	26	1.67	2.8	6.3	22.6	12.9	46.0	29.0	103.6
Steel 124		3.7	0.85	7.8	26	1.67	7.8	3.1	4.0	6.4	8.2	14.4	18.4
Steel 600		6.72	0.71	7.8	26	1.67	7.8	2.1	2.6	4.2	5.4	9.5	12.1
Steel 40		2.02	0.92	7.8	26	1.67	7.8	5.3	7.6	10.8	13.8	24.3	31.1
High hardness steel		3.45	0.87	7.8	26	1.67	7.8	3.3	4.2	6.7	8.6	15.1	19.4
Ti-alloy		3.23	0.85	7.8	26	1.67	4.6	3.6	7.7	7.3	15.8	16.4	35.6
SiC		22	0.35	7.8	26	1.67	3.1	1.3	4.2	2.6	8.5	5.9	19.1
6112	**Hardened steel, (HV_p = 6,55GPa, δ_{Hp}=0.75**	0.84	0.92	7.8	26	4.88	2.7	37.1	137.5	75.8	280.6	170.5	631.2
AMG5		0.8	0.93	7.8	26	4.88	2.7	38.6	142.8	78.7	291.5	177.1	655.9
8112		1.8	0.84	7.8	26	4.88	2.8	19.0	67.8	38.7	138.3	87.1	311.2
8312		1.9	0.82	7.8	26	4.88	2.8	18.4	65.8	37.6	134.2	84.6	302.0
Steel 124		3.7	0.85	7.8	26	4.88	7.8	9.1	11.7	18.6	23.9	41.9	53.7
Steel 600		6.72	0.71	7.8	26	4.88	7.8	6.0	7.7	12.3	15.7	27.6	35.4
Steel 40		2.02	0.92	7.8	26	4.88	7.8	15.4	19.8	31.4	40.3	70.7	90.7
High hardness steel		3.45	0.87	7.8	26	4.88	7.8	9.6	12.3	19.6	25.1	44.1	56.5
Ti-alloy		3.23	0.85	7.8	26	4.88	4.6	10.4	22.6	21.3	46.2	47.8	103.8
SiC		22	0.35	7.8	26	4.88	3.1	3.7 (4.8*)	12.1	7.6 (9.8*)	24.7	17.1	55.6
6112	**Hardened steel, (HV_p = 6,55GPa, δ_{Hp}=0.75**	0.84	0.92	7.8	51.6	4.88	2.7	73.7	272.9	150.4	557.0	338.4	1253.2
AMG5		0.8	0.93	7.8	51.6	4.88	2.7	76.5	283.5	156.2	578.5	351.5	1301.7
8112		1.8	0.84	7.8	51.6	4.88	2.8	37.7	134.5	76.9	274.5	172.9	617.7
8312		1.9	0.82	7.8	51.6	4.88	2.8	36.6	130.5	74.6	266.4	167.8	599.4
Steel 124		3.7	0.85	7.8	51.6	4.88	7.8	18.1	23.2	36.9	47.4	83.1	106.6
Steel 600		6.72	0.71	7.8	51.6	4.88	7.8	11.9	15.3	24.3	31.2	54.8	70.3
Steel 40		2.02	0.92	7.8	51.6	4.88	7.8	30.6	39.2	62.4	80.0	140.4	180.0
High hardness steel		3.45	0.87	7.8	51.6	4.88	7.8	19.1	24.4	38.9	49.9	87.5	112.2
Ti-alloy		3.23	0.85	7.8	51.6	4.88	4.6	20.6	44.9	42.1	91.6	94.8	206.1
SiC		22	0.35	7.8	51.6	4.88	3.1	7.4 (9.6*)	24.0	15.1 (19.6*)	49.0	34.0	110.3

* The values for the composite target with the ceramics/back thickness ratio 3:1 are shown in parenthesis

5. Maps of distribution of microhardness, plastic deformation and plasticity characteristic in targets after the impact loading

For investigation of deformation mechanism and strain hardening during impact loading and penetration, targets from alloys with different types of strengthening were used: steel 40, high hardness steel and Ti-alloy. Chemical compositions of alloys are given in the table 1.

Conditions of impact loading of targets from alloys are given in the part 1.

For investigation of the plastic deformation around the penetration channel the incompletely penetrated targets were selected. The targets were cut along the axis of moving of the kinetic energy projectile (KEP), and the Vickers microhardness (at a load of 2 N) was measured in the cut section. Typical maps of microhardness distribution are given in Fig.2, 4 and 5.

A modeling of the deformation process was carried out by compression of specimens, which were prepared from the same steels and Ti-alloy. The specimen size was 5x5x5 mm^3. The deformation curves in the coordinates compression stress σ_{comp} – plastic deformation ε_p are given in Fig.6. The microhardness was measured in the specimens, which were deformed to different deformation degrees. The dependence of microhardness on the deformation degree is given in Fig.7 as well.

The local plasticity characteristic of the material δ_H [65-67] was calculated for every point, in which microhardness was determined.

This plasticity characteristic has been introduced as a part of the plastic deformation in the total elastic-plastic deformation under the indenter

$$\delta_H = \frac{\varepsilon_p}{\varepsilon_t} = 1 - \frac{\varepsilon_e}{\varepsilon_t}. \qquad (10)$$

Here ε_p, ε_e and ε_t are the mean values of plastic, elastic and total deformation of the specimen on the contact area of the indenter with specimen in the loading direction; $\varepsilon_t = \varepsilon_p + \varepsilon_e$ and $\varepsilon_p \approx const$ when a pyramidal indenter is used for hardness measurement.

As it can be seen from Eq.(10), δ_H is a dimensionless parameter ranging from 0 (for "pure" elastic deformation) to 1 when the elastic deformation is insignificant. It was shown in [68], that elastic deformation is given by

$$\varepsilon_e = \frac{HM}{E_1} \cdot \left(1 - \nu_1 - 2\nu_1^2\right), \qquad (11)$$

where HM is the Meier hardness, E_1 is the Young modulus and ν_1 is the Poisson's ratio of the material.

Plastic deformation can be calculated from the ratio [66-68]:

$$\varepsilon_p = -\ln(\sin\gamma_2), \tag{12}$$

where γ_2 is the angle between the face of the hardness indentation pyramid and the loading direction. In this case $\gamma_2 > \gamma_1$, where γ_1 is an appropriate angle of diamond indenter. The angle γ_2 for pyramidal indenters can be defined from the ratio [66, 69]

$$ctg\gamma_2 = ctg\gamma_1 - 1.77\frac{HM}{E_{ef}}. \tag{13}$$

Here E_{ef} is the effective Young's modulus of the indenter – specimen contact couple, and

$$\frac{1}{E_{ef}} = \frac{1-\nu_1^2}{E_1} + \frac{1-\nu_2^2}{E_2}, \tag{14}$$

where E_2 and ν_2 are Young's modulus and Poisson ratio of the indenter.

The values of plasticity characteristic δ_H for investigated materials are given in the Figs.2, 4 and 5. Using the dependence $HV(\varepsilon_p)$ (Fig.7) as a calibration curve, the value of the conditional deformation ε_p was calculated for every point of target as well. Consequently, the maps of microhardness distribution in Fig.2, 4 and 5 are simultaneously the maps of plastic deformation distribution and distribution of the plasticity characteristic δ_H. The distribution of microhardness along the lines *0a*, *0b* and *0c* of target from steel 40 is given in Fig.3, the lines (*0a*, *0b* and *0c*) are plotted in Fig.2.

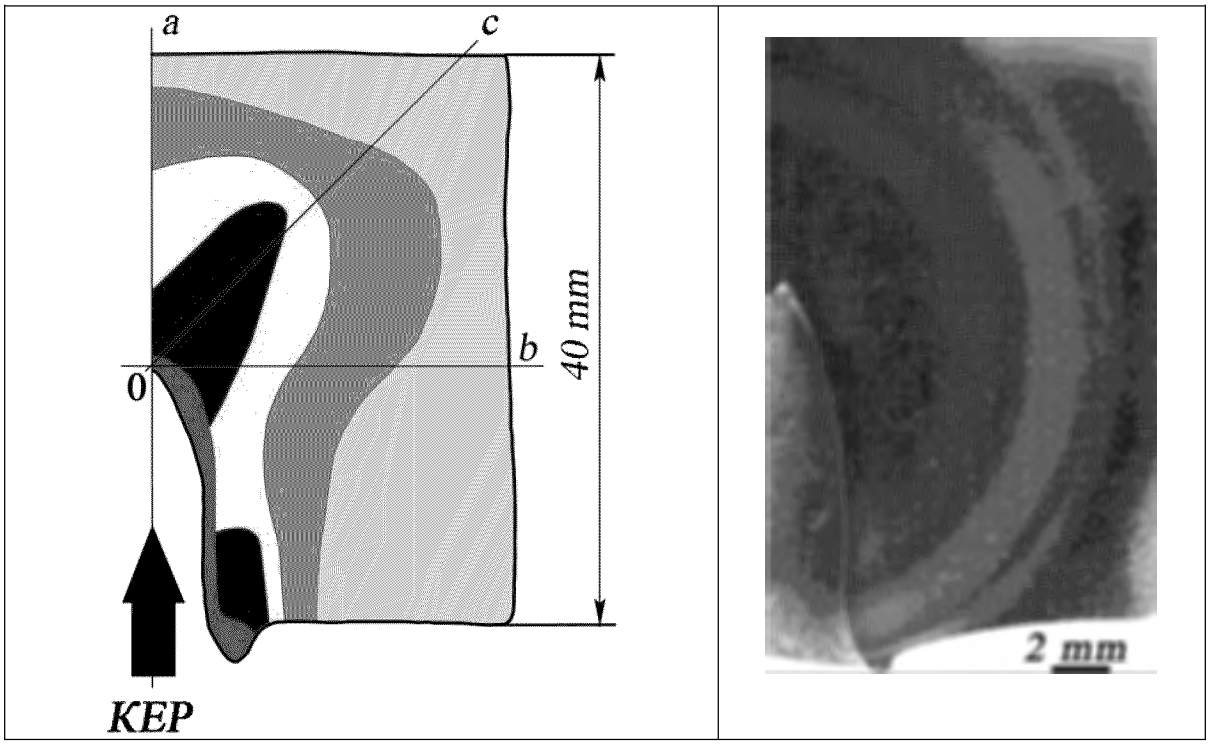

Area	HV, GPa	ε_p, %	δ_H
	2.8 ÷ 3.4	20 ÷ >40	0.89 ÷ 0.86
	2.5 ÷ 2.8	8 ÷ 20	0.90 ÷ 0.89
	2.2 ÷ 2.5	1.5 ÷ 8	0.91 ÷ 0.90
	2.0 ÷ 2.2	0.5 ÷ 1.5	0.92 ÷ 0.91
	1.9 ÷ 2.0	0 ÷ 0.5	~ 0.92

Fig 2 The target from steel 40, velocity of KEP V = 420 m/s.
The map of distribution of microhardness HV, the value of plastic deformation ε_p and plasticity characteristic δ_H after impact loading.

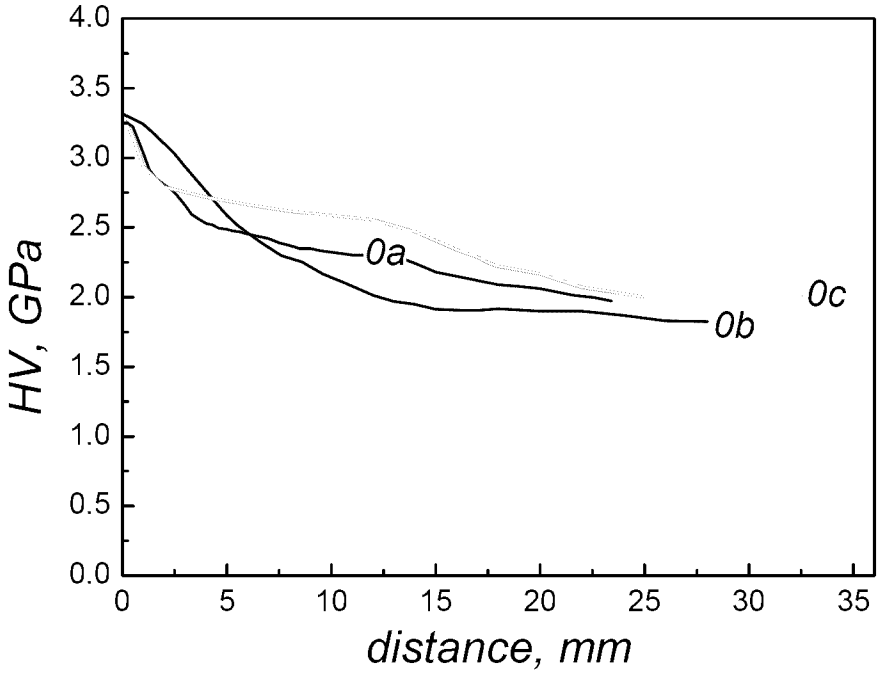

Fig 3 Microhardness along the lines *0a*, *0b* and *0c* of target from steel 40 (see Fig.2).

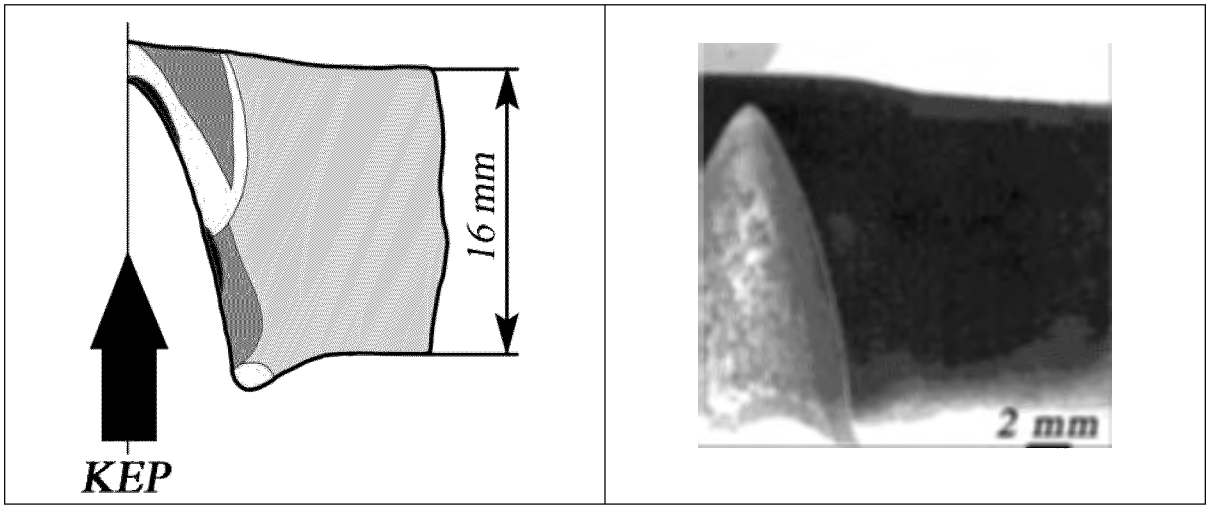

Area	HV, GPa	ε_p, %	δ_H
	4.5 ÷ 4.7	> 60	0.83 ÷ 0.82
	3.8 ÷ 4.5	15 ÷ 60	0.86 ÷ 0.83
	3.6 ÷ 3.8	1.5 ÷ 15	0.86 ÷ 0.86
	3.2 ÷ 3.6	0 ÷ 1.5	0.88 ÷ 0.86

Fig 4 The target from high hardness steel, velocity of KEP V = 468 m/s.
The map of distribution of microhardness HV, the value of plastic deformation ε_p and plasticity characteristic δ_H after impact loading.

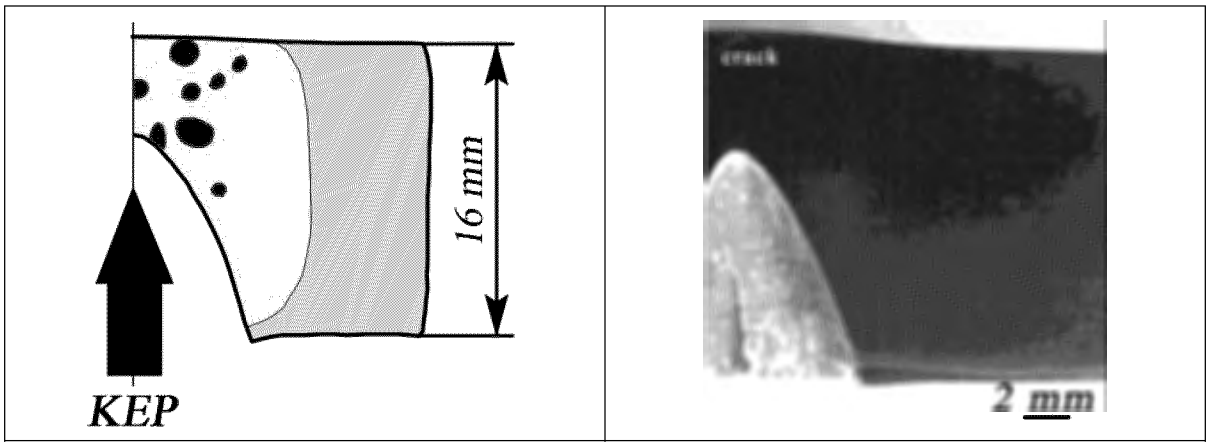

Area	HV , GPa	ε_p , %	δ_H
	3.8 ÷ 4.2	7 ÷ 22	0.81 ÷ 0.79
	3.3 ÷ 3.8	2 ÷ 7	0.84 ÷ 0.81
	3.2 ÷ 3.3	0 ÷ 2	~ 0.84

Fig 5 The target from Ti-alloy, velocity of KEP V = 274 m/s.
The map of distribution of microhardness HV , the value of plastic deformation ε_p and plasticity characteristic δ_H after impact loading.

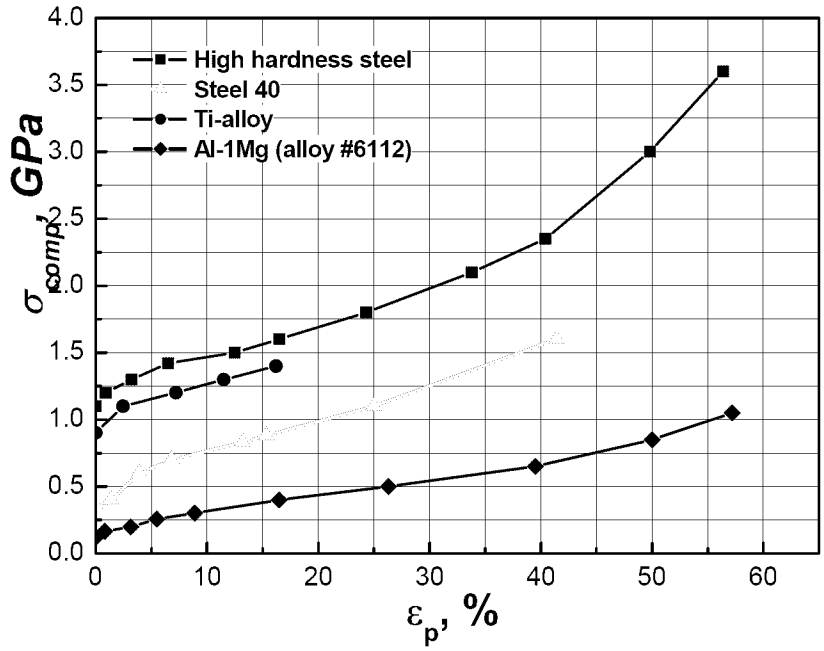

Fig 6 The influence of deformation degree ε_p on the compression stress σ_{compp} for static compression loading for different materials of targets.

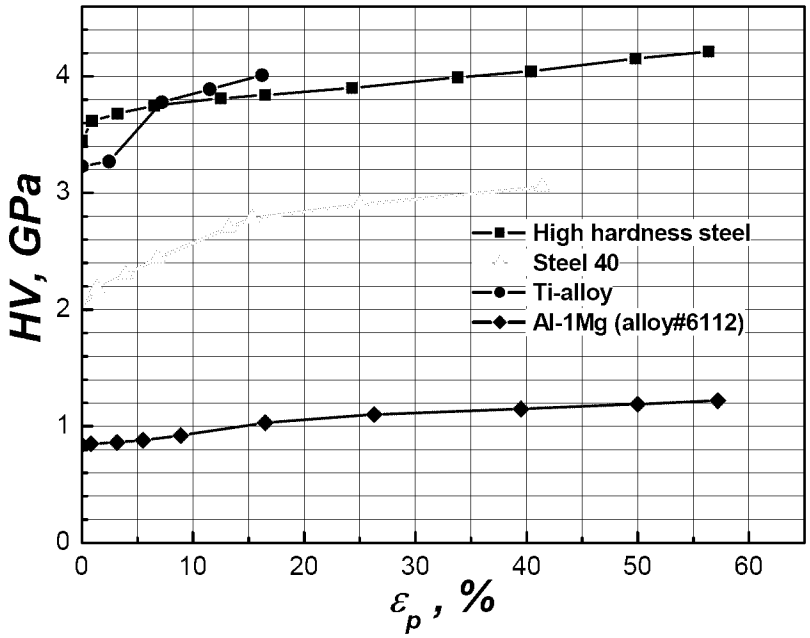

Fig 7 The influence of deformation degree ε_p on the microhardness HV for static compression loading for different materials of targets.

The value of plastic deformation during impact loading of a target by the KEP can be estimated from the Fig.2, 4 and 5. It is seen that plastic deformation is essential, and may be equivalent to 40-50 % of static plastic deformation for steels.

In the case steel 40 the deformed zone has more dimension in comparable with zones for high hardness and Ti-alloy. The hardness of the deformed zone increases and achieves the value HV = 3.4 GPa for steel 40 (Fig.2).

As it is seen from Fig.2, 4 the increasing of hardness around penetration channel for investigated steels achieves 50 %, that corresponds to plastic deformation ε_p=40-60 %. For target from Ti-alloy the plastic deformation around penetration channel is lower ($\varepsilon_p \approx$20 %) and at this deformation fracture is observed in dynamic and in static loading as well.

6. The energy expended for the plastic deformation

The method for estimation of the energy w_p expended for the plastic deformation of target during impact loading or penetration of KEP was proposed by authors in [64].

The energy expended for the plastic deformation of the target during penetration of the indenter may be estimated for every i-region in the map of Fig.2 as

$$w_i = 2\pi R_i S_i U_i . \qquad (15)$$

Here S_i is the surface of i-region in Fig.2 with approximately constant hardness H_i, R_i is the distance from the axis of the penetration channel to the centre of gravity of the i-region; U_i is the energy expended for plastic deformation of a unity of volume in the i-region.

It was assumed that U_i may be evaluated by equation

$$U_i = \int_0^{\varepsilon_{pi}} \sigma_i d\varepsilon_p = \frac{\overline{H_i} \cdot \overline{\varepsilon_{pi}}}{3}, \qquad (16)$$

where $\overline{H_i}$ and $\overline{\varepsilon_{pi}}$ are the average values of hardness and plastic deformation for the i-region.

The total energy expended for plastic deformation of target will be

$$w_p = \sum_i w_i . \qquad (17)$$

Calculation of w_p were fulfilled for steel 40. The kinetic energy of KEP was calculated as well ($w_k = \frac{mv^2}{2}$).

Table 5 The energy expended for the plastic deformation of targets during penetration of the indenter and kinetic energy of the KEP.

Material	V, m/s	w_k, J	w_p, J	w_p / w_k, %
Steel 40	420	2655	1338	~50

It is seen that the value of the energy expended for the plastic deformation of target during penetration of the KEP w_p is equal approximately 50 % of the kinetic energy of the KEP w_k. Other 50 % of the kinetic energy is expended for the heating, elastic vibration etc.

7. CONCLUSION

1. The theory enabling to calculate ballistic limit velocity V_{cr} of penetration of target by not deformable projectile is developed. Calculated and experimental data are in a good agreement.
2. The semi-empirical formula allowing to calculate ballistic limit velocity V_{cr} both for not deformable and deformable projectile, at different ratio of mechanical properties of projectile and target is suggested. Values of hardness and plasticity characteristic δ_H defined at indentation and introduced by authors are employed in calculations for characteristic of mechanical properties. As targets we investigated different metals (steels, aluminum and titanium alloys) as well as ceramics. As projectile materials we applied soft and hardened steels.
   The obtained experimental results are in a good agreement with calculations made under the suggested formula.
   The estimation of critical thickness of target for different types of projectile and various velocities of their movement is carried out.

3. By critical specific surface weight of targets the investigated materials can be arranged in the following order in line with growth of density of target per surface unit $(\rho h)_{t\,cr}$ (when $V_{cr} = const$):
   - soft aluminum alloys,
   - high-strength aluminum alloys
   - soft steel,
   - titanium alloy,
   - high-strength steels,
   - ceramics
4. The maps of distribution of microhardness, plastic deformation and plasticity characteristic in targets from aluminum alloys and steels after impact loading were obtained.
   The energy expended for the plastic deformation around the KEP in the case of its stopping in the steel targets ($V < V_{cr}$) is approximately 50 % from the KEP kinetic energy.

References

1. Sagomonian AJ. Penetration. Moscow: Moscow State Univ. Publ. House, 1974 (in Russian).
2. Sagomonian AJ. Impact and penetration of solids into fluid. Moscow: Moscow State Univ. Publ. House, 1986 (in Russian).
3. Voejkov IV, Sagomonian AJ. Penetration of brittle fractured barrier by a rigid cone. Izv. AN USSR. Mechanics of solid body 1985;6:182-4 (in Russian)
4. Aloyan MA. Penetration of a thin rigid cone in brittle material with supersonic speed. Izv. AN Armenian SSR. Mechanics 1985;38(5):12-21 (in Russian).
5. Liapykhin PP, Zhurahovskij SV, Ivaschenko KB. A law of penetration of thick plates of low-deformable long cores, Problems of Strength 1993;10:63-70 (in Russian).
6. Bahrah SM, Kovalev NP, Fedorov YuG. On penetration of rigid sphere in elastic-plastic and viscous mediums with back pressure. Math. Modeling 1992;4(12):21-3 (in Russian).
7. Forrestal MJ, Okajima K, Luk VK. Penetration of 6061-T651 aluminum targets with rigid long rods. ASME J. of Appl. Mech 1988;55:755-60.
8. Forrestal M.L., Luk V.K., Rosenberg Z., Brar N.S. Penetration of 7075-T651 aluminum targets with ogival-nose rods. Int. J. Solids Struct. 1992;29:1729-1736.
9. Forrestal MJ, Piekutowski AJ. Penetration experiments with 6061-T651 aluminum targets and spherical-nose steel projectiles at striking velocities between 0.5 and 3.0 km/s. Int J Impact Eng 2000;24:57-67.
10. Dikshit SN, Sundararajan G. The penetration of thick steel plates by ogive shaped projectiles-experiment and analysis. Int. J. Impact Engng 1992;12(3): 373-408.
11. Piekutowski AJ, Forrestal MJ, Poormon KL, Warren TL. Penetration of 6061-T6511 Aluminum targets by ogive-nose steel projectiles with striking velocities between 0.5 and 3.0 km/s. Int. J. Impact Engng 1999;23:723-34.
12. Warren TL, Forrestal MJ. Effects of strain hardening and strain-rate sensitivity on the penetration of aluminum targets with spherical-nose rods. Int. J. Solids Struct. 1998;35:3737-52.
13. Warren TL. Simulations of the penetration of limestone targets by ogive-nose 4340 steel projectiles. Int J Impact Eng 2002;27:475-96.
14. Yossifon G, Rubin MB, Yarin AL. Penetration of a rigid projectile into a finite thickness elastic-plastic target – comparison between theory and numerical computations. Int. J. Impact Engng 2001;25(3):265-90.
15. Chen XW, Li QM. Deep penetration of a non-deformable projectile with different geometrical characteristics. Int. J. Impact Engng 2002;27(6):619-37.
16. Yarin AL, Rubin MB, Roisman IV. Penetration of a rigid projectile into an elastic-plastic target of finite thickness. Int. J. Impact Engng 1995;16(5-6):801-31.
17. Roisman IV, Yarin AL, Rubin MB. Oblique penetration of a rigid projectile into an elastic-plastic target. Int. J. Impact Engng 1997;19(9-10):769-95.
18. Gabov SA. Introduction in the theory of nonlinear waves. Moscow: Moscow State Univ. Publ. House, 1988 (in Russian).
19. Loytsyanskii LG. Mechanics of Fluid and Gas. Moscow: Nauka Publ., 1978 (in Russian).
20. Galanov BA, Ivanov SM, Kartuzov VV. On one new modification of Alekseevskii-Tate model for nonstationary penetration of long rods into targets. Int. J. Impact Engng 2001;26(1-10):201-10.
21. Hill R. The Mathematical Theiry of Plasticity. Oxford: Clarendon Press, 1985.
22. Tate A. Long rod penetration model - Part II. Extentions to hydrodynamic theory of penetration. Int. J. Mech. Sci. 1986;28(9):599-612. 2. Satapathy S., Bless S.J. Calculation of penetration resistance of brittle materials using spherical cavity expansion analysis. Mech. Materials, 23(4)(1996)323-330
23. Satapathy S, Bless S. Calculation of penetration resistance of brittle materials using spherical cavity expansion analysis. Mech. Materials, 1996;23:323-30.
24. Frew DJ, Forrestal MJ, Hanchak SJ. Penetration experiments with limestone targets and ogive-nose steel projectiles. ASME Journal of Applied Mechanics, 2000; 67:841-845.
25. Brebbia CA, Netlles JCF, Wrobel LC. Boundary Element Techniques. Theory and Applications in Engineering. Berlin, Heidelberg: Springer-Verlag, 1984.

26. Dwight H.B. Tables of integrals and other mathematical data. 6-th ed. Moscow: Nauka Publ., 1983 (in Russian).
27. Timoshenko S. Vibration problems in engineering. Toronto: D.Van Nostrand Company, 1955.
28. Goldsmith W. Impact. The theory and physical behaviour of colliding solids. London: Arnold, 1960.
29. Johnson KL. Contact mechanics. Cambridge: Cambridge University Press, 1985.
30. Timoshenko S. Stability of elastic systems. Moscow–Leningrad: OGIZ. State publishing house of technico-theoretical literature, 1946.
31. Frew DJ, Forrestal MJ, Cargile JD. The effect of concrete target diameter on projectile deceleration and penetration depth. Int. J. Impact Engng 2006;32:1584-94.
32. Masket AV. The measurement of forces resisting armor penetration. J. Appl. Phys. 1949;20:132-140.
33. Satapathy S. Application of cavity expansion analysis to penetration problems IAT.R0136, Institute for Advanced Technology, University of Texas, May 1997.
34. Normandia M.J. Impact response and analysis of several silicon carbides. Int. J. Appl. Ceram. Technol. 1(3)(2004)226-234
35. Shtern M.B., et al. Phenomenological theories of powder pressing. Kiev, Naukova dumka, 1982. 140 p.
36. Skorokhod V.V. Rheological foundations of theory of sintering. Kiev, Naukova dumka, 1972. 152 p.
37. Shtern M.B. Model of deformation processes in compressible materials taking into account pore formation. I. Constitutive equations and loading surface. Powder metallurgy, 5(1985)28-34
38. Shtern M.B. Model of deformation processes in compressible materials taking into account pore formation. II. Uniaxial tension and compression of porous bodies. Powder metallurgy, 6(1985)34-39
39. Petrov J.V. Quantum analogy in fracture mechanics of solid bodies // FTT. 1996. - 38, № 11 – pp. 3385-3393.
40. Grandson M.P. A model of cohesion zones in view of triaxial parameter // Mesomechanics. **2001.-4,** №4 – pp. 9-19.
41. Barenblatt G.I. Mathematical theory of equilibrium cracks in brittle fracture // Advances in Applied Mechanics – Academic Press, 1962.-v. 7. – p.55-79.
42. Uemura Y. Atomistic model for evaluation of stability of diamond under uniaxial tensile force // Phys. Rev. B. - **1994.-49.** № 10. - p. 6528-6538. Atomistic simulation of behavior of diamond under compressive stress // Phys. Rev. B. - **1995.-51.** № 10. - p. 6704-6706
43. Telling R.H., Pickard C.J., Payne M.C., Field J.E. Theoretical strength and cleavage of diamond // Physical review Letters. 2000.-84, № 22 – P. 5160-5169.
44. Weixue Li, Truchinag Wang. Elasticity, stability, and ideal strength of $\beta - SiC$ in plane – wave – based **ab initio** calculations // Physical review B. 1999. – **59**, № 6 – P. 3993-4001.
45. Rondy David, Cohen Marvin L. Ideal strength of diamond, SiC and Ge // physical review B. 2001. – **64**, № 21 – P. 212103/1-212103/3.
46. Zakarjan D.A., V.V. Investigation of strength characteristics of titanium on the basis of calculation of energy of interaction between densely packed atomic planes // In proceedings Mathematical models and computing experiment in material science. Works of IPMS NASU. **2003.-6,** pp. 59-66.
47. Piljankevich A.N., Zakarjan D.A. Modeling of pseudo-potential. 2. Diamond and $BN_{сф}$ // Ukrainian physical journal. - 1986. – **31,** № 1. – pp. 93-96.
48. Zakarjan D.A., V.V. Calculation of theoretical strength of diamond-like materials, proceeding from energy of interaction of atomic planes Reports of NASU. 2006.-№ 7, pp. 94-99.
49. Kheyne V., Cohen M., Uer D. Theory of pseudo potential.-M.: Mir, 1973.- p.557
50. Evans A., Hur A., D. Fracture toughness of ceramics. In book Mechanics of destruction. № **17.** Fracture of materials. Izd., Mir. Moscow 1979г. p. 238.
51. Gruzkov A.A., Krivosheev S.I., Petrov Yu.V. Power consumption of fracture of materials in conditions of impulse loading of microsec time // FTT. - **45,** № 5 - pp. 842-845.

52. Tomlinson P.N., Pipkin N.J., Lammer A., Burnancl R.P. High performance of drilling – syndax 3 shocos versatility // Jndustrial diamond revien 6/85 (JDR.) – 1985. – **45**, № 511. – P. 3299-3304.
53. Futergendler S.I., Druj M.S. Structure and mechanical properties of single crystals of cubic boron nitride at annealing in vacuum Super hard materials. 1983. - № 4.–C. 13-16.
54. Novikov N.V., Dub S.N., Malnev V.I. Microhardness and crack resistance of single crystals of cubic boron nitride Superhard materials. – 1983. - № 5. – pp. 16-20.
55. Gusev A.M. Effect of nanocrystalline conditions in compact metals and compositions // UFN - 1998.- vol.168.-№2.- pp.55-82.
56. Joiners B.B., Salamgariv H. Sh. Methodical features of definition of mechanical properties of ultrafine-grained materials // Physics of metals and metallurgical science. – 2005, т. 100.-№ 3.- with. 109-114.
57. Nagaev E.L. Small metal particles // UFN 1992. – vol.-162, - № 9.- pp. 49-121.
58. Bamard A.S., Zapol P. A model for phase stability of arbitrary nanoparticles as a function of size and shape // J. Of Chemical Physics, 2004.-v.121, № 9.-p. 4276-4283.
59. Smirnov V.M. Clusters with dense packing // UFN, 1992. – т. 162, № 1. – pp. 119-162.
60. Andrievsky R.A. Production and properties of nanocrystalline refractory compounds // Successes of Chemistry, 1994. – T. 63, № 5. – pp. 431-448.
61. Krivtsov A.M., Frosts H.Ф. About mechanical characteristics of nanosized objects // FTT, 2002.- T. 44, №12.- pp.2158-2163
62. Loboda O.S., Krivtsov A.M. Influence of scale factor on modules of elasticity three-dimensional nanocrystal // Fur. A solid body, 2005.-№4.- pp.27-41.
63. Petrov Yu.I. Physics of small particles. Moscow, Nauka, 1982 pp. 358.
64. Yu.V.Milman, S.I.Chugunova, I.V.Goncharova, V.A.Goncharuk, N.A.Yefimov. Physics of deformation and fracture at impact loading and penetration. Impact Eng., v.10, 2006.
65. Yu.V.Milman, B.A.Galanov, and S.I.Chugunova. Plasticity Characteristic Obtained through Hardness Measurement. Acta Met. and Mater., (overview No.107), No.9, 1993, p.2523-2532.
66. B.A.Galanov, Yu.V.Milman, S.I.Chugunova, and I.V.Goncharova. Investigation of mechanical properties of high-hardness materials by indentation. Superhard Materials, v.3,1999, p.25-38.
67. Yu.V.Milman. New Methods of Micromechanical Testing of Materials by Local Loading with a Rigid Indenter. In: Advanced Materials Science: 21st Century, ed: Cambridge International Science Publishing, 1998, p.638-659.
68. Yu.V.Milman, S.I.Chugunova. Mechanical Properties, Indentation and Dynamic Yield Stress of Ceramic Targets. International Journal of Impact Engineering, v.23, No.1, 1999, p.629-638.
69. Yu.V.Milman, W.Gooch, I.I.Timofeeva, S.I.Chugunova, and I.V.Gridneva. Pressure Induced Phase Transition in Ceramic Materials during Indentation. CP505, Shock Compression of Condensed Matter – 1999, ed:M.D.Furnish, L.C.Chhabildas and R.S.Hixson, American Institute of Physics, 2000, p.251-254.